University Library

MINERVA ACCESS

A gateway to Melbourne's research publications

Minerva Access is the Institutional Repository of The University of Melbourne

Author/s:
Van Bergen, NJ;Ahmed, SM;Collins, F;Cowley, M;Vetro, A;Dale, RC;Hock, DH;De Caestecker, C;Minal, M;Massey, S;Gladys, H;Pisano, T;Glover, S;Gusman, J;Stroud, DA;Dinger, M;Guerrini, R;MacAra, IG;Christodoulou, J

Title:
Mutations in the exocyst component EXOC2 cause severe defects in human brain development

Date:
2020-01-01

Citation:
Van Bergen, N. J., Ahmed, S. M., Collins, F., Cowley, M., Vetro, A., Dale, R. C., Hock, D. H., De Caestecker, C., Minal, M., Massey, S., Gladys, H., Pisano, T., Glover, S., Gusman, J., Stroud, D. A., Dinger, M., Guerrini, R., MacAra, I. G. & Christodoulou, J. (2020). Mutations in the exocyst component EXOC2 cause severe defects in human brain development. Journal of Experimental Medicine, 217 (10), https://doi.org/10.1084/JEM.20192040.

Persistent Link:
https://hdl.handle.net/11343/277755

License:
CC BY-NC-SA

JEM Journal of Experimental Medicine

ARTICLE

Mutations in the exocyst component EXOC2 cause severe defects in human brain development

Nicole J. Van Bergen[1,2*], Syed Mukhtar Ahmed[3*], Felicity Collins[4,5], Mark Cowley[6,7,8], Annalisa Vetro[9], Russell C. Dale[10,11], Daniella H. Hock[12], Christian de Caestecker[3], Minal Menezes[13], Sean Massey[1], Gladys Ho[4], Tiziana Pisano[9], Seana Glover[1,2], Jovanka Gusman[1,2], David A. Stroud[12], Marcel Dinger[6,14], Renzo Guerrini[9], Ian G. Macara[3**], and John Christodoulou[1,2,15**]

The exocyst, an octameric protein complex, is an essential component of the membrane transport machinery required for tethering and fusion of vesicles at the plasma membrane. We report pathogenic variants in an exocyst subunit, *EXOC2* (*Sec5*). Affected individuals have severe developmental delay, dysmorphism, and brain abnormalities; variability associated with epilepsy; and poor motor skills. Family 1 had two offspring with a homozygous truncating variant in *EXOC2* that leads to nonsense-mediated decay of *EXOC2* transcript, a severe reduction in exocytosis and vesicle fusion, and undetectable levels of EXOC2 protein. The patient from Family 2 had a milder clinical phenotype and reduced exocytosis. Cells from both patients showed defective Arl13b localization to the primary cilium. The discovery of mutations that partially disable exocyst function provides valuable insight into this essential protein complex in neural development. Since EXOC2 and other exocyst complex subunits are critical to neuronal function, our findings suggest that *EXOC2* variants are the cause of the patients' neurological disorders.

Introduction

Vesicle transport plays a crucial role in the development of the brain and is central to the function of all neurons and glia. Neurotransmitter release at synapses is the dominant activity of mature neurons, but vesicle traffic is also vital for outgrowth and maintenance of axons, for synaptogenesis, and synaptic plasticity. Neurotransmitter receptors and transporters, ion channels, and cadherins all require targeted transport to specific regions of the neuronal plasma membrane (Burack et al., 2000; Gärtner et al., 2015; Kelly and Grote, 1993). The delivery of post-Golgi vesicle cargo to the plasma membrane requires an initial vesicle tethering step, followed by fusion to the membrane (Bröcker et al., 2010; Dubuke and Munson, 2016; Sztul and Lupashin, 2006). The major tethering factor is a protein complex called exocyst. Neurotransmitter release from synaptic vesicles is, at least in *Drosophila*, independent of exocyst, but the complex is required for all other known types of vesicles, including the insertion of AMPA receptors into the postsynaptic membrane (Murthy et al., 2003). Exocyst is also needed for dendrite arbor formation and spine maturation in hippocampal neurons (Lira et al., 2019; Vega and Hsu, 2001). Components of the exocyst complex are enriched in actin-containing growth cones, synaptic boutons, and filopodia (Hazuka et al., 1999; Koon et al., 2018). When filopodia are suppressed, axons become disorientated (Bentley and Toroian-Raymond, 1986; Chien et al., 1993), and consistent with a guidance role, filopodia are critical to the migration of neuronal growth cones (Letourneau, 1981).

The exocyst complex is conserved throughout most eukaryotic organisms and consists of eight subunits that are organized

[1]Brain and Mitochondrial Research Group, Murdoch Children's Research Institute, Royal Children's Hospital, Melbourne, Victoria, Australia; [2]Department of Paediatrics, University of Melbourne, Melbourne, Victoria, Australia; [3]Department of Cell and Developmental Biology, Vanderbilt University School of Medicine, Nashville, TN; [4]Western Sydney Genetics Program, Children's Hospital at Westmead, Sydney, New South Wales, Australia; [5]Medical Genomics Department, Royal Prince Alfred Hospital, Sydney, New South Wales, Australia; [6]Kinghorn Centre for Clinical Genomics, Garvan Institute of Medical Research, Sydney, New South Wales, Australia; [7]St Vincent's Clinical School, University of New South Wales Sydney, Sydney, New South Wales, Australia; [8]Children's Cancer Institute, Kensington, New South Wales, Australia; [9]Pediatric Neurology, Neurogenetics and Neurobiology Unit and Laboratories, Meyer Children's Hospital, University of Florence, Florence, Italy; [10]Department of Paediatric Neurology, The Children's Hospital at Westmead, Sydney, New South Wales, Australia; [11]Kids Neuroscience Centre, Faculty of Medicine and Health, The University of Sydney, Sydney, New South Wales, Australia; [12]Department of Biochemistry and Molecular Biology and The Bio21 Molecular Science and Biotechnology Institute, The University of Melbourne, Parkville, Victoria, Australia; [13]Kids Research, The Children's Hospital at Westmead, Sydney, New South Wales, Australia; [14]School of Biotechnology and Biomolecular Sciences, University of New South Wales, Kensington Campus, Sydney, New South Wales, Australia; [15]Victorian Clinical Genetics Services, Royal Children's Hospital, Parkville, Victoria, Australia.

*N.J. Van Bergen and S.M. Ahmed contributed equally to this paper; **I. Macara and J. Christodoulou contributed equally to this paper; Correspondence to John Christodoulou: john.christodoulou@mcri.edu.au; Ian G. Macara: ian.g.macara@vanderbilt.edu.

© 2020 Van Bergen et al. This article is distributed under the terms of an Attribution–Noncommercial–Share Alike–No Mirror Sites license for the first six months after the publication date (see http://www.rupress.org/terms/). After six months it is available under a Creative Commons License (Attribution–Noncommercial–Share Alike 4.0 International license, as described at https://creativecommons.org/licenses/by-nc-sa/4.0/).

into two subcomplexes (SCs) of four subunits each (Heider et al., 2016; Mei and Guo, 2018). SC1 consists of EXOC1, EXOC2, EXOC3, and EXOC4. SC2 consists of EXOC5, EXOC6, EXOC7, and EXOC8. In humans, three closely related proteins, EXOC3, EXOC3L1, and EXOC3L2, have cell type–specific expression; however, there are no other isoforms of EXOC2. In budding yeast, each of the eight exocyst subunits is structurally similar, with a long N-terminal α-helical region (the CorEx motif) that engages in coiled-coil interactions with the CorEx motif of a second subunit and a C-terminal region of short antiparallel helical bundles (Mei et al., 2018). The basic structure of a mammalian exocyst is likely to be similar, but the amino acid sequences of the human subunits are only ∼25% similar to those in yeast, and two of them (EXOC2 and EXOC8) bind to the small GTPases RalA and RalB (Fukai et al., 2003; Jin et al., 2005; Mott et al., 2003), which are not present in yeast; thus, substantial differences in regulation of the complex likely exist. Indeed, although the yeast exocyst is believed to be a stable octamer, the mammalian complex, by contrast, is in a dynamic equilibrium between free subunits, SCs, and the intact octamer (Ahmed et al., 2018). However, when and where they assemble relative to the arrival of exocytic vesicles at the plasma membrane remains to be established, and the molecular function of the exocyst complex in tethering and fusion remains unknown.

Consistent with an essential function in membrane traffic, exocyst loss of function (LoF) is lethal in yeast, *Caenorhabditis elegans*, *Drosophila,* and mice and in multiple cell lines (Armenti et al., 2014; Friedrich et al., 1997; Murthy et al., 2003, 2005; Roumanie et al., 2005; Wu et al., 2010). Remarkably, however, mutations in some subunits are tolerated. Budding yeast can survive LoF mutations of *EXOC1* (Finger and Novick, 1997; Novick et al., 1980), for example, and in *Drosophila,* a truncation mutant of *EXOC2* that retains the CorEx motif allows organismal viability (Sommer et al., 2005; Wan et al., 2019). Exocyst function is also important for proper delivery to the primary cilium of the Joubert syndrome protein Arl13b and for ciliogenesis in a wide range of cell and tissue types. Mutations or loss of exocyst function has been linked to ciliopathy (Fogelgren et al., 2011; Lipschutz, 2019; Lobo et al., 2017; Rogers et al., 2004; Seixas et al., 2016; Zuo et al., 2009, 2019). The identification of partially disabling mutants of the mammalian exocyst would be particularly valuable by providing new tools to probe biological function.

Here, we report on two unrelated families with pathogenic variants in *EXOC2*. Affected individuals had developmental delay, dysmorphism, and brain abnormalities that in certain instances were associated with seizures and poor motor skills. By whole exome sequencing (ES), we identified pathogenic variants in *EXOC2* (RefSeq accession no. NM_018303.6) that were homozygous in affected children from Family 1 [c.1309C>T; p.Arg437*] and compound heterozygous in the affected child from Family 2 [c.389G>A; p.Arg130His and c.1739T>C; p.Leu580Ser]. Analysis of patient fibroblasts revealed reduced EXOC2 protein level in Family 1, impaired secretory vesicle fusion with the plasma membrane and defective bulk exocytosis, and impaired Arl13b localization to the primary cilium. Based on genetic and functional genomics findings, we suggest that the *EXOC2* variants we have identified are the cause of the neurological disorder in these patients.

Results

Patient descriptions

Here, we report on two unrelated families with pathogenic variants in the exocyst subunit *EXOC2*. Family 1 is a large consanguineous family with multiple children of Lebanese background. Affected individuals from two sub-branches in Family 1 were born after uncomplicated pregnancies; however, both sub-branches of Family 1 had reported miscarriages of unknown cause. Affected children had progressive microcephaly, congenital cataracts, severe global developmental delay, seizures, severe intellectual disability, and facial dysmorphism (Table 1). Patient 1 also had epilepsy. Brain magnetic resonance imaging (MRI) showed hypoplastic cerebellum and brainstem, white matter loss, thinning of the corpus callosum, severely hypoplastic hippocampi, and hypoplastic optic cups (Fig. 1, A–L). For additional clinical details see Materials and methods, Detailed patient reports section, and Table S1. One of the affected children is deceased, while the other requires full-time care. Family 2 had a child born to a nonconsanguineous Italian family. She had mild intellectual disability, dysmorphism, mild obstructive sleep apnea syndrome, and poor fine and gross motor skills, and MRI revealed a "molar tooth" midbrain malformation and an abnormal structure of the cerebellar cortical pattern (Fig. 1, M–R).

In summary, the brain malformation is much more severe in Patients 1 and 2, but the malformation complex leading to the molar tooth sign is more visible in Patient 3. It is likely that the brainstem–cerebellar malformation in Patients 1 and 2 is too severe to generate a molar tooth–shaped appearance of the pons and cerebellar peduncles, as these structures are hypoplastic. Patients 1 and 2 have a number of additional abnormalities.

Sequencing and in silico analysis

ES analysis identified pathogenic variants of the *EXOC2* gene in affected individuals from both families. Affected Patients 1 and 2 in Family 1 were confirmed to be homozygous for the c.1309C>T, p.Arg437* variant (chr6:g.576766G>A, hg19) by Sanger sequencing, while their parents were heterozygous for this variant and unaffected siblings were either heterozygous for the variant or homozygous for the wild-type variant (Fig. 2 A), consistent with autosomal recessive inheritance. According to the Genome Aggregation Database (gnomAD), five heterozygotes and no homozygotes were reported for the c.1309C>T variant in Family 1, with a global minor allele frequency (MAF) of 1.77e-5, according to gnomAD (allele count 5/282,474, heterozygous in Finnish and non-Finnish European populations).

The affected patient in Family 2 was confirmed to be compound heterozygous for two *EXOC2* variants: c.[389G>A]; [1739T>C] p.[(Arg130His)];[(Leu580Ser)]. Each parent was heterozygous for one of the variants each (Fig. 2 B). The global MAF of the c.389G>A variant was 7.96e-05, according to gnomAD (allele count 6/251,314, heterozygous in non-Finnish European and Latino populations, no homozygotes reported), whereas the

Table 1. **Clinical summary of affected family members with *EXOC2*-related neurological disorder**

	Family 1	Family 1	Family 2
Individual	Patient 1:IV-2 (Patient 1)	Patient 1:IV-8 (Patient 2)	Patient 2:II-1 (Patient 3)
EXOC2 variants	NM_018303.6:c.1309 C>T p.Arg437*	NM_018303.6:c.1309 C>T p.Arg437*	NM_018303.5:c.389G>A p.Arg130His and c.1739T>C, p.Leu580Ser
Gender	Male	Female	Female
Age at onset	Birth	Birth	4 mo
Age at death	10 yr	Alive	Alive
Acquired microcephaly (HP:0004485)	+	+	–
Severe global developmental delay (HP:0001263)	+	+	Borderline intellectual functioning
Spastic quadriplegia (HP:0001258)	+	+	–
Congenital contractures of joints (HP:0001371)	+	+	–
Epilepsy (HP:0001250)	+	–	–
Facial dysmorphism (HP:0001999)	Small sloping forehead (HP:0000340), upslanting palpebral fissures (HP:0000582), high broad nasal bridge (HP:0000431), broad depressed nasal tip (HP:0000437), long flat philtrum (HP:0000319), and thin upper lip (HP:0000219)	Sloping forehead (HP:0000340), hypertelorism (HP:0000316), upslanting palpebral fissures (HP:0000582), broad depressed nasal bridge (HP:0005280), and broad depressed nasal tip (HP:0000437)	At age 6 yr, 3 mo: oval face (HP:0000300) with slight bitemporal depression (HP:0025386), high forehead (HP:0000348), arched eyebrows (HP:0002553), hypertelorism (interpupillary distance at the 97th centile; HP:0000316), low-set simplified ears (HP:0000369), thin upper lip (HP:0000219) with Cupid's bow, lateralized nipples, and slightly dry skin (HP:0000958)
MRI	Hypoplastic inferior cerebellar vermis and cerebellar hemispheres (HP:0001320), large fourth ventricle (HP:0002119), decreased supratentorial white matter volume and thinning of corpus callosum (HP:0002079), and normal pituitary bright spot	Hypoplastic optic discs (HP:0007766), generalized decreased myelination (HP:0012447), frontal horn cysts (HP:0030724), fusion of thalami (HP:0010664), and hypoplastic brainstem (HP:0002365) and cerebellum (HP:0001321)	Molar tooth cerebellar abnormality (HP:0002419) associated with vermis hypoplasia (HP:0001320) and rhombencephalosynapsis (HP:0031913)
Other	Ventricular septal defect (HP:0001629)	–	Small accessory spleen (HP:0010451) and obstructive sleep apnea syndrome (HP:0002870)

c.1739T>C variant was not reported in that database. Examining the gnomAD database for all *EXOC2* variants in control populations, a total of 42 predicted LoF variant positions were reported (combined allele count of 97/10,295,746; combined MAF of 9.42e-06; no homozygote LoF variants reported), and 428 predicted missense variant positions were reported. There was a total combined missense allele count of 3,120/102,355,114; combined MAF of 3.05e-05. Regarding homozygous missense variants, only seven individuals were reported in gnomAD. The seven individuals had one of three homozygous missense variants, and all were benign (Polyphen2). These seven individuals with benign homozygous missense variants were from an African (n = 6) or South Asian (n = 1) population. Table S3 and Table S4 provide biallelic variants from exome data of Patients 2 and 3, respectively.

To determine whether the c.1309C>A variant led to *EXOC2* transcript undergoing nonsense-mediated decay, patient and control fibroblasts were cultured in the presence or absence of cycloheximide before cDNA synthesis and quantitative RT-PCR (qRT-PCR). A significant decrease in relative levels of *EXOC2* transcripts was observed in fibroblasts from Patient 2, which was partially restored back to control levels in the presence of cycloheximide. The *EXOC2* c.1309C>T variant renders the *EXOC2* transcript sensitive to nonsense-mediated decay. There was no significant decrease in *EXOC2* transcript levels in Patient 3 compared with controls (Fig. 2 C).

The protein variants from both Family 1 and Family 2 are in highly conserved regions of the protein (Fig. 2 D).

EXOC2 protein level is reduced in cells derived from Patient 2

The transcript harboring the homozygous *EXOC2* c.1309C>T variant is subject to nonsense-mediated decay, and the variant is predicted to result in a frameshift and early truncation of the EXOC2 protein p.Arg437*. Western blot analysis using an

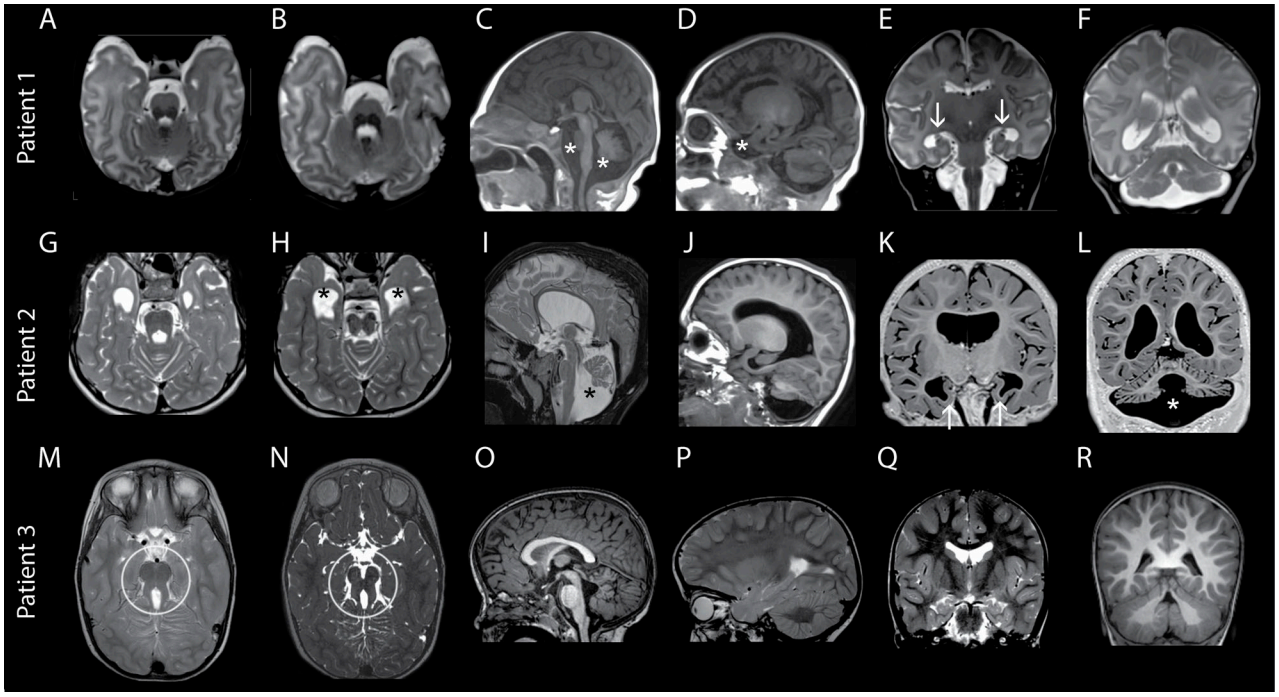


Figure 1. **Clinical and brain imaging features of affected patients with *EXOC2*-related neurological disorder. (A–F)** Patient 1 (1:IV-2): In the axial sections, the pons and fourth ventricle have an abnormal shape, which is only in part reminiscent of the molar tooth appearance; there is ponto-cerebellar and brainstem hypoplasia (asterisks in C), with more severe involvement of the inferior vermis with respect to the other cerebellar structures; narrow isthmus (not shown here); severely hypoplastic under-rotated hippocampi (downward pointing arrows in E); thin corpus callosum with cavum septi and large ventricles; and midline thalamic fusion and hypoplastic caudate nuclei. Microcephaly was also noted, with dilated subarachnoid spaces in correspondence with the temporal poles (asterisk in D). **(G–L)** Patient 2 (1:IV-8): The same observations apply as in Patient 1, but all observations are more severe. In particular, the brainstem and cerebellum are severely hypoplastic (asterisk in I and L), and the hippocampi are barely visible on both sides (see asterisks in H and upward-pointing arrows in K). The septum pellucidum is absent. Mild generalized atrophy is noted. **(M–R)** Patient 3 (2:II-1): Molar tooth–shaped pons and fourth ventricle in the axial sections (encircled in M and N); narrow isthmus; cerebellar vermis hypoplasia; cleft separating the two dysplastic areas of the vermis; rhombencephalosynapsis and vertical orientation of the folial pattern; and under-rotated hippocampi.

antibody against EXOC2 detected full-length EXOC2 protein in control fibroblasts (predicted size of 104 kD; Fig. 3 A), but it was completely absent in Patient 2 fibroblasts. The p.(Arg487*) variant is predicted to form a smaller 48-kD protein, which was not detected using an antibody against the N-terminal region of EXOC2, which would be expected to detect the truncated protein. Analysis of EXOC2 protein abundance in Patient 3 demonstrated no reduction in protein levels (Fig. 3 B).

Similar to fibroblasts, when protein levels were measured in isolated peripheral blood mononuclear cells (PBMCs) from affected individuals in Family 1, no EXOC2 protein was detected; however, EXOC2 protein levels in a parent (Patient 1:III-4) and an unaffected sibling (Patient 1:IV-7) or in controls were normal (Fig. 3 C). For functional experiments, fibroblasts were transduced with *EXOC2* lentiviral particles to restore EXOC2 protein levels, and transduced cells were selected with puromycin. Cultures of untransduced cells were maintained in parallel. EXOC2 protein levels were restored back to control levels in Patient 2 fibroblasts, while EXOC2 protein levels in control fibroblasts and Patient 3 remained unchanged (Fig. 3 D).

Since complete absence of EXOC2 protein is predicted to be embryonic lethal, we further examined fibroblasts from an affected individual in Family 1 and the affected individual in Family 2 compared with four control fibroblast lines using tandem mass tag (TMT) multiplexed quantitative mass spectrometry (Table S2). As can be seen in Fig. 3 E, EXOC2 was the most strongly reduced protein in Patient 2 fibroblasts compared with the mean from four control cell lines. The abundance of EXOC2 and housekeeping proteins GAPDH and VDAC2 was not highly variable in either control (Fig. 3 F), indicating the robustness of the data. Additionally, the level of EXOC3 was also significantly altered (>1.5-fold change) in Patient 2 fibroblasts, with other EXOC proteins also in lower abundance but to a lesser extent (Fig. 3, E and F). In contrast, the cellular levels of EXOC2 and the other EXOC proteins were unaltered in Patient 3 fibroblasts (Fig. 3, G and H).

Expression of EXOC2 is required for fibroblast survival

To test whether Patient 2 fibroblasts could tolerate a complete disruption of EXOC2 expression, we used lentiviral CRISPR/Cas9 gene editing with guide RNAs targeting exon 2 (containing the initiation start codon) of the EXOC2 gene and assessed cell death by DAPI uptake. Knockout of *EXOC2* in both wild-type and Patient 2 fibroblasts caused substantial cell death within 3 d after transduction compared with untransduced wild-type cells (Fig. 4 A). From this result, we infer that the low level (greater than fourfold lower than control) of truncated EXOC2 expressed in Patient 2 fibroblasts is sufficient to maintain viability.

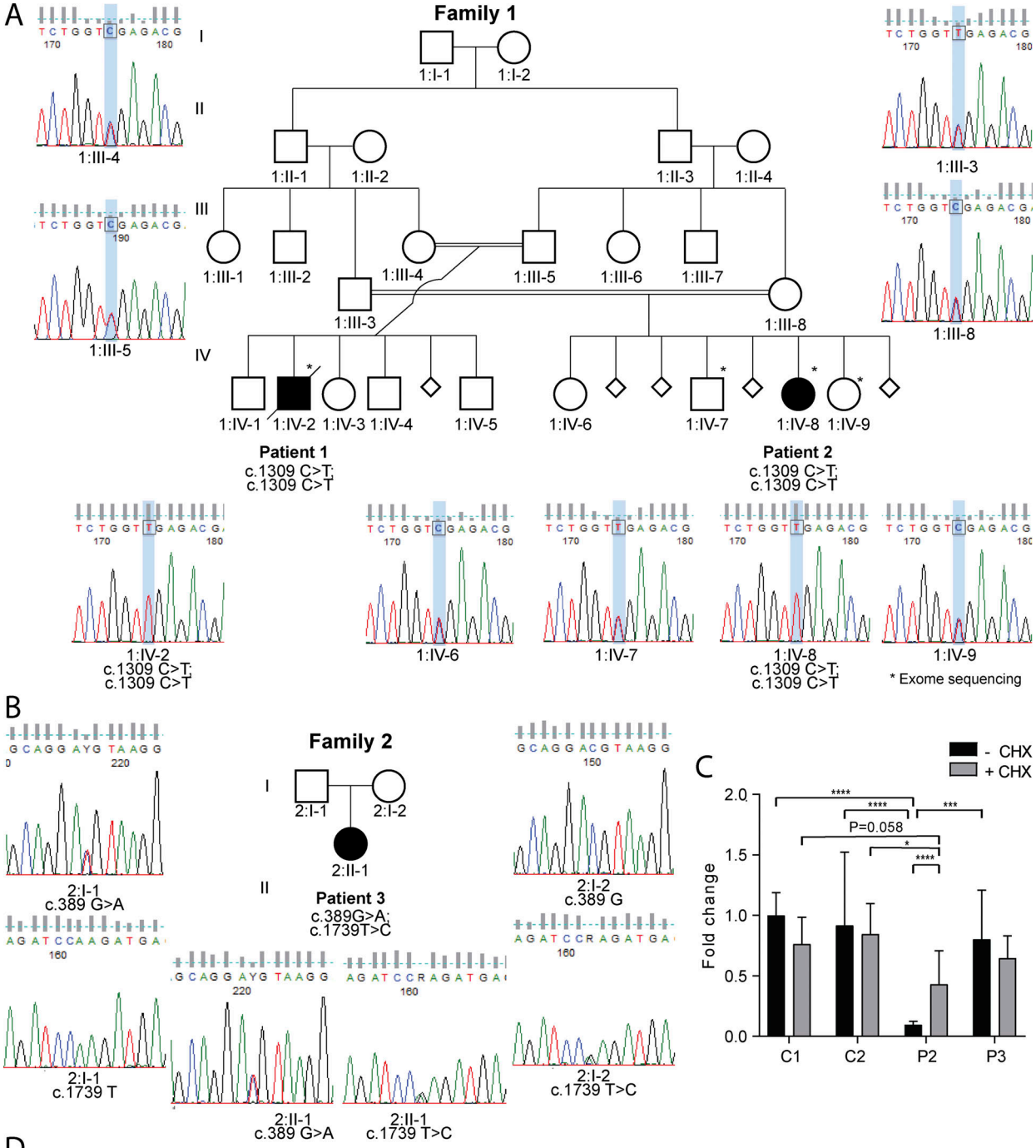


Figure 2. **Pedigrees of families and genetic findings in EXOC2-deficient families. (A)** Pedigrees of Families 1 and 2 and confirmatory Sanger sequencing. Family 1 has a homozygous c.1309C>T; p.Arg437* *EXOC2* variant in the affected patients, a heterozygous variant in each parent, and homozygous wild-type or heterozygous configuration in unaffected tested siblings. **(B)** The affected individual in Family 2 has compound heterozygous variants [c.389G>A; p.Arg130His and c.1739T>C; p.Leu580Ser] with one allele inherited from each parent. **(C)** qRT-PCR in control (C1 and C2) and patient (P2 and P3) fibroblasts showed a significant decrease in *EXOC2* transcript abundance in Patient 2 fibroblasts compared with controls. Cycloheximide treatment (+CHX) prevented nonsense-mediated decay and partially restored transcript abundance in Patient 2 fibroblasts. Transcript abundance in Patient 3 was comparable to that of controls.

(D) Multiple sequence alignment of EXOC2 and related proteins was performed using the Multiz Alignment of 100 vertebrates. The pathogenic *EXOC2* variants are in highly conserved regions (highlighted in yellow). Asterisk indicates ES. Data in C are mean ± SD; $n > 3$ per measurement from at least three biological collections of each cell line, duplicate qPCR reactions, and representative of two independent *EXOC2* primer pairs and normalized against three housekeeper genes. Statistical significance was determined using two-way ANOVA with Sidak correction for multiple comparisons versus sample C1. *, $P < 0.05$; **, $P < 0.01$; ***, $P < 0.001$; ****, $P < 0.0001$.

As an orthogonal approach, we created a mutation similar to that of Patient 2 in a normal murine mammary gland cell line. This line expresses endogenously tagged Exoc7-sfGFP, which is in SC2 (Ahmed et al., 2018). A guide RNA was used to target exon 14 of the Exoc2 locus so as to create mutations by CRISPR/Cas9–mediated nonhomologous end joining. Nonsense mutations in this exon would be predicted to truncate the protein product, resulting in an ∼48-kD N-terminal fragment. We then probed cell lysates for Exoc2. As shown in Fig. 4 B, a fraction of these cells was successfully edited and expressed a truncated protein of ∼48 kD (Fig. 4 B). Because the cell population was polyclonal, full-length Exoc2 protein was also present from cells in which only one allele or neither allele was successfully edited. Using these cells, we next performed a coprecipitation assay using GFP-Trap beads to purify Exoc7-GFP and measured association with the full-length and truncated fragment of Exoc2. Strikingly, both the full-length and, to a lesser extent, the truncated fragment of Exoc2 were bound to Exoc7-GFP (Fig. 4 B). These data demonstrate that an N-terminal fragment of Exoc2, which contains the CorEx domain, can be expressed in cells and is able to associate with exocyst SC2.

EXOC2 truncation does not affect the stoichiometry of EXOC4–EXOC7 interaction

Previously, we had found that loss of either Exoc4 or Exoc1 in normal murine mammary gland cells destabilizes the entire SC1, which consists of EXOC1–4, preventing their binding to SC2 (Ahmed et al., 2018). Therefore, we next asked if the mutant EXOC2 of Patient 2 impacts binding of EXOC4 to EXOC7. Cell lysates from control and Patient 2 fibroblasts were subjected to immunoprecipitation using EXOC7 antibody and blotted for EXOC4. Surprisingly, there was no significant decrease in coprecipitated EXOC4 from the Patient 2 fibroblasts compared with the control cells (Fig. 4 C).

The Rho GTPase GEF-H1 also interacts with the exocyst and was previously shown to directly bind to EXOC2 (Pathak et al., 2012). Hence, we tested whether GEF-H1 can interact with the exocyst from Patient 2 fibroblasts. Interestingly, immunoprecipitated EXOC7 was associated with similar amounts of GEF-H1 from wild-type and Patient 2 fibroblasts, suggesting that, despite the very low level of truncated EXOC2, GEF-H1 can still associate with exocyst (Fig. 4 D).

Assessment of vesicle fusion rates in patient fibroblasts

Depletion of exocyst subunits from cell lines by RNA interference or gene editing strongly reduces the efficiency of global vesicle fusions to the plasma membrane, measured using VAMP2-pHluorin (Ahmed et al., 2018). Therefore, we asked if the *EXOC2* variants described above also impact vesicle fusion rates. VAMP2-pHluorin is a v-SNARE fusion to a pH-sensitive GFP that marks the majority of exocytic vesicles in a cell and becomes highly fluorescent only upon vesicle fusion with the plasma membrane (Xu et al., 2011). Control, Patient 2, and Patient 3 fibroblasts were transiently transfected with VAMP2-pHluorin, and fusions were assessed using total internal reflection fluorescence microscopy (TIRFM; Fig. 5, A–D). The fusion rate was calculated as the number of fusions per unit area per second. Representative 3D kymographs are shown in Fig. 5 A, in which sudden, short bursts of fluorescence denote fusion events. Fusion rates were significantly reduced (by >50%) in Patient 2 fibroblasts harboring the p.Arg437* variant compared with control human fibroblasts; however, no significant change in global fusion rates was detected for fibroblasts from Patient 3 with compound heterozygous *EXOC2* variants (Fig. 5, A and B). To test if the reduction in vesicle fusion rate for Patient 2 fibroblasts is causally related to the mutation in EXOC2, we performed a rescue experiment. Confirming this hypothesis, lentiviral expression of EXOC2 restored the protein to wild-type levels (Fig. 5 C) and increased vesicle fusions by approximately twofold (Fig. 5 D).

Altered vesicular stomatitis virus glycoprotein (VSVG)–GFP surface exposure in fibroblasts from affected patients

We next probed the impact on specific cargo delivery by the pathogenic *EXOC2* variants. We used a temperature-sensitive form of VSVG fused to GFP (VSVG-GFP ts045) as a well-validated marker protein for transport along the secretory pathway and exocytosis (Ahmed and Macara, 2017; Liljedahl et al., 2001; Ren and Guo, 2012; Yeaman et al., 2001). This protein construct misfolds at higher temperatures (40°C) and accumulates in the ER. When cells are returned to permissive temperature (32°C), the construct exits the ER and is transported via the Golgi to the plasma membrane (Bergmann and Singer, 1983). The construct normally reaches the cell surface after 60–120 min (Hirschberg et al., 1998). To examine the final fusion of VSVG-GFP with the plasma membrane, immunostaining was performed on nonpermeabilized cells for an epitope on the extracellular domain of VSVG using the monoclonal 8G5 antibody (Lefrancois and Lyles, 1982). We transfected fibroblasts with the VSVG-GFP ts045 construct, held them at the restrictive temperature (40°C) overnight, and then shifted them to the permissive temperature (32°C), synchronously triggering release from the ER. To quantify fusion efficiency, cells were fixed at regular intervals and then counterstained with 8G5 (Fig. 5, E–I). The amount of VSVG-GFP protein on the surface was normalized to the total amount of VSVG-GFP protein in the cells. Notably, the amount of VSVG-GFP detected by 8G5 on the plasma membrane was significantly reduced in both Patient 2 and Patient 3 fibroblasts compared with control fibroblasts (Fig. 5 E).

To confirm that exocytosis is delayed by the *EXOC2* variants, we performed rescue experiments. Lentiviral transduction of

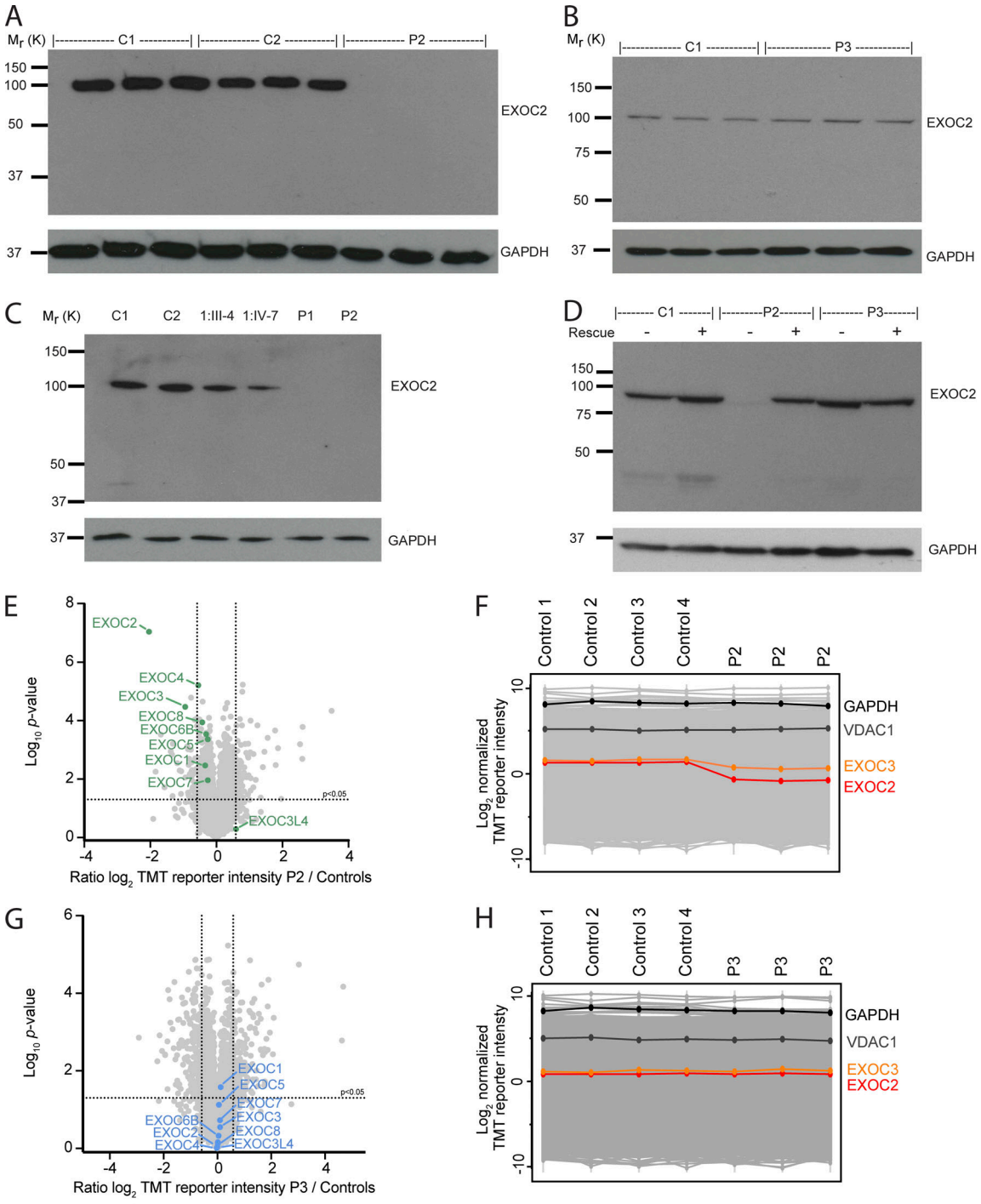


Figure 3. **Decreased protein levels in fibroblasts and PBMCs from an affected patient with *EXOC2* p.Arg437* homozygous variant. (A)** Western blot of EXOC2 and GAPDH levels in fibroblasts from two pediatric controls (C1 and C2) as well as in fibroblasts from Patient 2 (P2) with c.1309C>T. p.Arg437* *EXOC2* homozygous variant in triplicate shows undetectable protein levels in Patient 2. **(B)** Western blot of EXOC2 and GAPDH in fibroblasts from Patient 3 (P3) in Family 2 with compound heterozygous variants in *EXOC2* showed no reduction in EXOC2 protein levels. **(C)** Western blot of EXOC2 and GAPDH in PBMCs from two healthy controls (C1 and C2), two clinically unaffected children from Family 1 (1:III-4 and 1:IV-7) who are heterozygous for the c.1309C>T; p.Arg437* *EXOC2* variant, and two affected individuals, Patients 1 and 2 (P1 and P2) from Family 1 who are homozygous for the c.1309C>T; p.Arg437* *EXOC2* variant shows undetectable levels of EXOC2 protein in affected individuals. **(D)** Fibroblasts were either untransduced (–) or transduced (+) with wild-type EXOC2 by lentivirus, which restored protein levels in Patient 2. No increase in EXOC2 levels were seen in control or Patient 3 (P3) fibroblasts after lentiviral transduction. **(E)** Volcano plot depicting the results from a two-sample two-sided *t* test between TMT reporter values in Patient 2 (P2) replicates versus four controls. The horizontal line depicts a P value of 0.05, and the vertical lines represent fold changes of 1.5. **(F)** Profile plots of $\log_2$-transformed normalized TMT reporter intensities for cellular proteins in Patient 2 (P2) and control fibroblasts. GAPDH and VDAC1 are shown as control proteins. **(G)** As for E, but relating to Patient 3 (P3). **(H)** As for F, but relating to Patient 3 (P3). Data in A and B represent three biological collections from each cell line, experiment performed twice. Data in C and D represent a single biological collection per patient sample, experiment performed twice. Data in E and G represent pooled biological triplicates for the

patient fibroblast cell lines and four pooled independent control fibroblast lines with a single biological collection for each. The global proteomics experiment was performed once for each TMT-labeled pool (pool A = panels E and F, pool 2 = panels G and H). Data in F and H represent each biological sample for the two TMT-labeled pools.

wild-type *EXOC2* into control fibroblasts had no impact on exocytosis (Fig. 5 G). However, expression of wild-type *EXOC2* in fibroblasts from Patient 2 restored protein levels back to that of control fibroblasts and completely reversed the level of VSVG-GFP exocytosis to that of control cells (Fig. 5, F and H). Interestingly, lentiviral transduction with wild-type *EXOC2* into fibroblasts from Patient 3 did not restore their exocytosis defect (Fig. 5 I); however, basal EXOC2 protein levels were not reduced in this patient (Fig. 3 D). These experiments suggest that there is an exocytosis defect that can be explained by the truncation and reduced levels of EXOC2 protein in Patient 2, but in Patient 3 the compound missense variants appear to interfere dominantly with exocytosis.

EXOC2 variants affect ciliogenesis in patient fibroblasts

The molar tooth midbrain malformation manifested by Patient 3 suggests that developmental defects that could be related to ciliopathy (Martin-Urdiroz et al., 2016; Valente et al., 2013). Exocyst subunits are known to localize to the basal body and primary cilium, and loss of exocyst function has been linked to ciliopathy (Fogelgren et al., 2011; Nihalani et al., 2019; Rogers et al., 2004; Zuo et al., 2009). Therefore, we asked if cilia formation is affected in fibroblasts derived from patients with *EXOC2* mutations. We serum-starved the cells for 24–48 h and stained for acetylated α-tubulin to mark primary cilia. Surprisingly, there was no significant change in the fraction of ciliated cells between control and Patient 2 cells. A slight decrease was detected between control and the Patient 3 variant (Fig. 6, A and B), but this is likely a cell line–specific phenotype, as introduction of exogenous EXOC2 did not elevate cilia number (Fig. 6 B). Additionally, we detected no significant difference in cilia length between the variants and control fibroblasts (Fig. 6, C and D). Finally, we examined the localization of Arl13b to the primary cilium. Arl13b was previously reported to interact with EXOC2 and EXOC4 (Seixas et al., 2016). Arl13b localization to the cilia of Patient 2 and Patient 3 cells was reduced by ∼30% and ∼50%, respectively, compared with control cells (Fig. 6, F and G). This localization defect was rescued to wild-type levels upon exogenous expression of full-length wild-type EXOC2 (Fig. 6, E–G). We note that overexpression of EXOC2 in control cells reduced the localization of Arl13b to the cilia. We suggest that this effect is the result of excess EXOC2 subunit that cannot integrate into the complex, but which can independently associate with Arl13b (Seixas et al., 2016) and may prevent its proper localization to

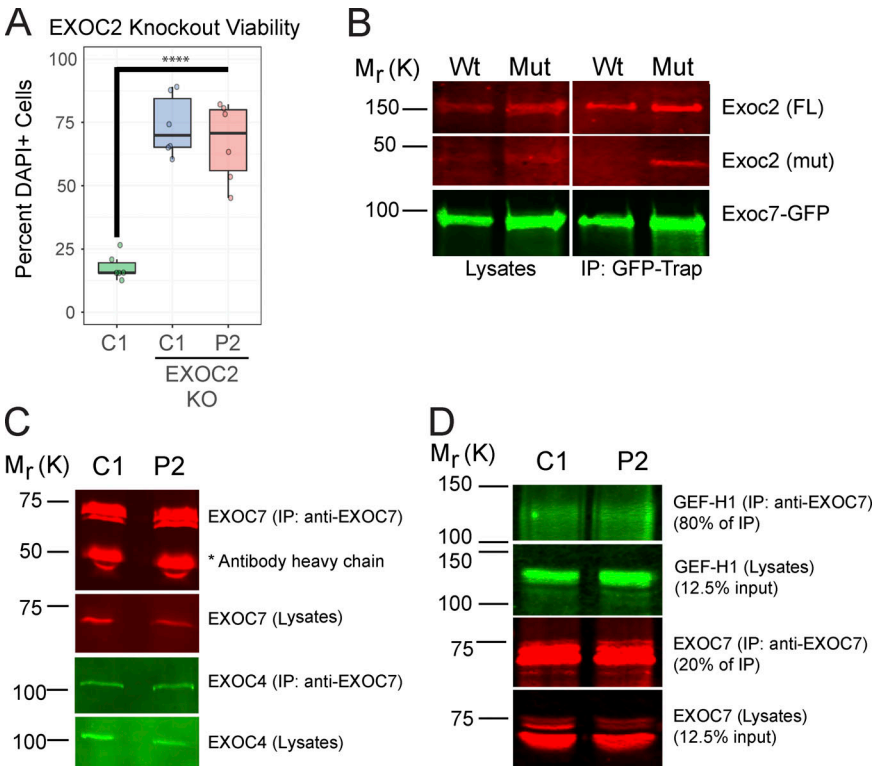


Figure 4. **Total loss of EXOC2 is lethal, and the truncated form of EXOC2 helps to retain hexameric exocyst complex. (A)** Viability of cells upon *EXOC2* gene knockout (KO) was assessed. Control (C1) or Patient 2 (P2) cells were mock transfected or transfected with sgRNA targeting exon 2 of *EXOC2* (EXOC2 KO). The number of live versus dead cells was assessed 3 d after transfection using DAPI staining. A representative of four experiments is shown. ****, $P < 0.0001$. **(B)** Interaction of truncated mouse Exoc2 with Exoc7-GFP. Exoc7-GFP was purified using GFP-Trap beads and immunoblotted using anti-Exoc2 and anti-GFP antibodies. Wt = Exoc7-GFP + Exoc2-HaloTag; Mut = Exoc7-GFP + Exoc2 truncated. Immunoprecipitation (IP) was performed from polyclonal population of Exoc2-truncated cells where a fraction of the cells was heterozygous. Whereas 77%–80% of Exoc2 (FL) was bound to Exoc7-GFP, 53% of truncated Exoc2 (mut) coprecipitated with Exoc7-GFP. Representative of three experiments. **(C)** Interaction between human EXOC7 and EXOC4 in control (C1) and Patient 2 (P2) fibroblasts. Cell lysates were subjected to immunoprecipitation with anti-Exoc7 antibodies and blotted for EXOC7 and EXOC4. Asterisk indicates antibody heavy chains at 50 kD. Representative of three experiments. **(D)** GEF-H1 binding to the exocyst was assessed in cell lysates upon immunoprecipitation of EXOC7 from control (C1) or Patient 2 (P2) fibroblasts. Representative of three experiments. In A, error bars indicate IQR, and line indicates median. P values were calculated using one-way ANOVA and Tukey post hoc analysis. Molecular weight standards are indicated on the left (kilodaltons).

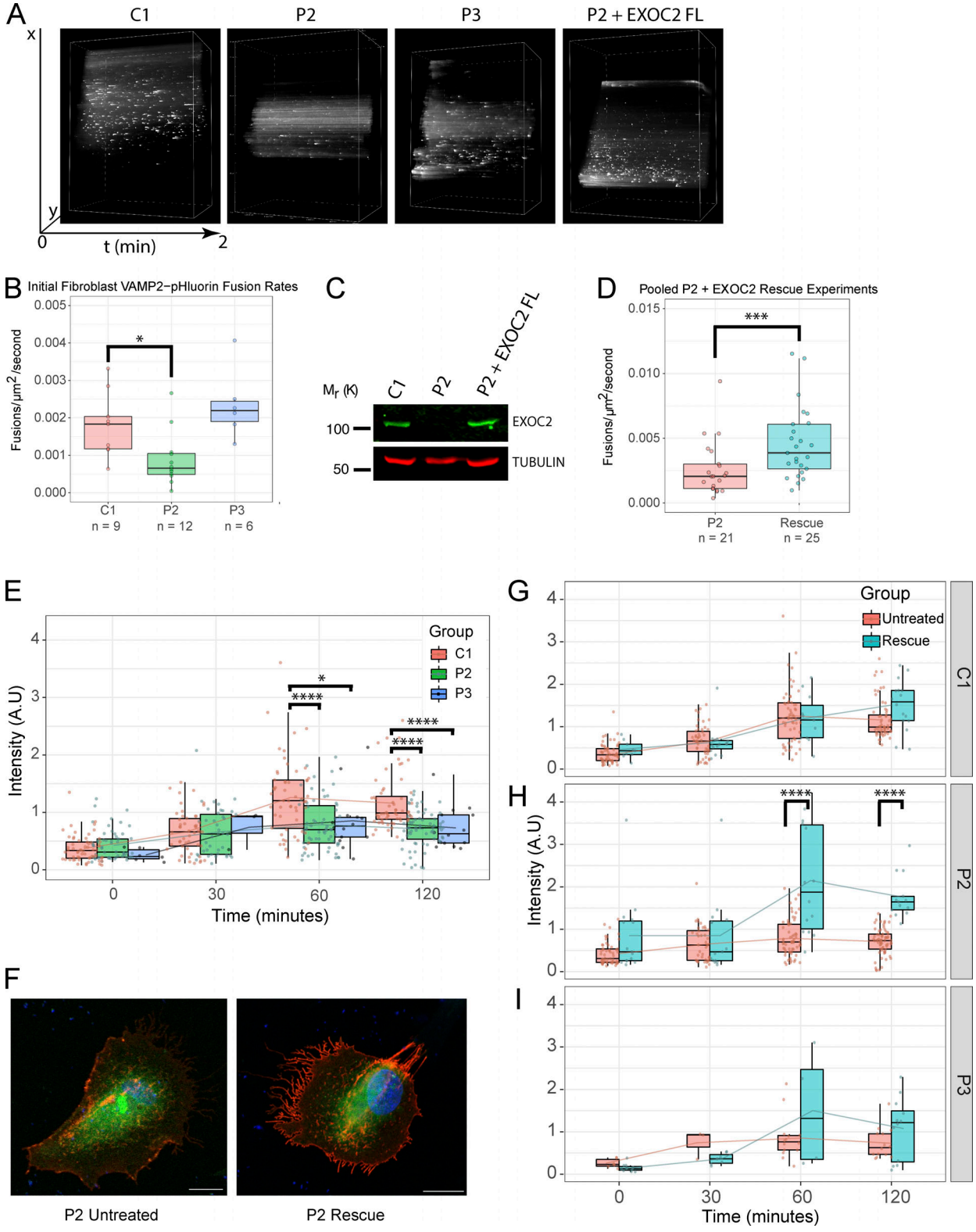


Figure 5. **Impaired plasma membrane trafficking in fibroblasts from affected patients is rescued by lentiviral transduction of wild-type *EXOC2*. (A)** Representative 3D kymographs showing vesicle fusions over time in the entire cell for each condition indicated. Images were recorded over 2 min with 180-ms intervals and 70-ms exposure using TIRFM. **(B)** Vesicle fusion rates calculated for control (C1), Patient 2 (P2), and Patient 3 (P3) fibroblasts as fusion per unit area (µm²) per second. Experiments were replicated at least three times, and a representative experiment is shown. Error bars indicate IQR, and line indicates median. P values were calculated using one-way ANOVA and Tukey post hoc analysis. P value for the statistics between C1 and P2 is 0.048; C1 to P3 is 0.423. Total number of fusions per cell in control, Patient 2, and Patient 3 fibroblasts was plotted against cell surface area. **(C)** Expression level of lentivirally expressed EXOC2 protein in fibroblasts from Patient 2 compared with wild-type cells. **(D)** Vesicle fusion rates calculated for Patient 2 fibroblasts that were mock

transfected or overexpressing EXOC2. P value was calculated using Student *t* test. Experiments were repeated three times, and pooled data are shown. P = 0.0094. **(E)** Control fibroblasts and fibroblasts derived from an affected individual from Family 1 and Family 2 were transfected with a VSVG-GFP ts045, then immunostained with the VSVG surface marker 8G5 and counterstained with the nuclear marker DAPI. VSVG-GFP ts045 relative intensity to 8G5 was calculated to represent exocytosis. There was a significant decrease in the exocytosis rate in fibroblasts from Patient 2 (P2) and Patient 3 (P3) compared with control (C1) fibroblasts. **(F)** Representative images of untreated and EXOC2-rescued fibroblasts from Patient 2: blue, DAPI; green, VSVG-GFP ts045; red, 8G5. **(G)** Control fibroblasts were either untreated or stably transduced with wild-type *EXOC2* lentivirus (EXOC2). There was no difference in exocytosis between naive control cells and those transduced with *EXOC2* lentivirus. **(H)** Exocytosis in fibroblasts from Patient 2 in Family 1 was restored back to levels of control fibroblasts upon transduction with wild-type *EXOC2* lentivirus. **(I)** Exocytosis in fibroblasts from Patient 3 was unchanged upon transduction with wild-type *EXOC2* lentivirus; however, endogenous protein levels were normal (Fig. 3 B). Data in E and G–I are median ± IQR. Significance was measured by two-way ANOVA with Sidak multiple comparisons correction. *, P < 0.05; ***, P < 0.001; ****, P < 0.0001. Scale bar = 20 µm. Representative of three experiments.

the cilium. We conclude that while ciliogenesis in the EXOC2 variant cells appears normal, Arl13b recruitment to the cilia is compromised by mutations in EXOC2.

Discussion

This work expands the number of exocyst genes associated with human disease, where we identify the first patients with pathogenic variants in *EXOC2*. The affected patients manifested a variable association of early-onset seizures, variable intellectual disability, microcephaly, sensorineural hearing loss, and developmental brain abnormalities, including a characteristic molar tooth midbrain malformation revealed by brain MRI. To our knowledge, there are no other reported pathogenic variants in human *EXOC2*, and the only disease associations for the exocyst complex are for *EXOC8* (MIM: 615283) and *EXOC4* (MIM: 608185). *EXOC8* was found to harbor a pathogenic homozygous variant in a single case report of a boy diagnosed with Joubert syndrome (Dixon-Salazar et al., 2012). Joubert syndrome is a neurodevelopmental disorder characterized by a molar tooth formation on brain imaging, with an underlying classical ciliopathy phenotype (Doherty, 2009). More recently, heterozygous *EXOC4* variants have been linked to nephrotic syndrome in patients (Nihalani et al., 2019).

In affected individuals from Family 1 exhibiting a severe neurological condition, a homozygous variant (c.1309C>T p.Arg437*) leads to nonsense-mediated decay of *EXOC2* transcripts, undetectable EXOC2 protein, and impaired exocytosis and vesicle fusion, which can be rescued by expression of wild-type *EXOC2*. In the affected individual from Family 2 with compound heterozygous variants in *EXOC2* (c.389G>A; p.Arg130His and c.1739T>C; p.Leu580Ser), transcript and protein levels were normal, but exocytosis (measured by tsVSVG-GFP surface exposure) was impaired. However, no significant defects in global steady-state vesicle fusions could be demonstrated using VAMP2-pHluorin. This difference might reflect a less severe defect that becomes more penetrant upon increased demand for membrane fusions, as occurs when tsVSVG-GFP is synchronously released from the ER. Interestingly, the defect in exocytosis of VSVG-GFP occurred even though EXOC2 levels are normal and was not rescued by transduction with wild-type *EXOC2*. Possibly, the compound heterozygous missense mutations are dominant over wild-type *EXOC2*, or cells may not allow overexpression of *EXOC2* as previously suggested (Rivera-Molina and Toomre, 2013). We are confident these "rescued" cells were successfully transduced with the lentiviral vector carrying the wild-type *EXOC2*, as cells were maintained under puromycin selection for 16 d after transduction, and in parallel cultures treated with puromycin, all cells died off after 3–4 d. Notably, expression of the exogenous wild-type EXOC2 was observable in fibroblasts from Patient 2. An additional consideration is that the milder phenotype of Patient 3 compared with Patient 2 could partially be explained by the less severe exocytosis defect as measured in fibroblasts.

We also discovered that the pathogenic mutations in *EXOC2* affect proper localization of Arl13b to primary cilia, possibly caused by delayed recruitment to the cilia or defective tethering by mutant exocyst. We did not find any defects in cilia number or length. However, it is possible that localization of ciliary membrane proteins such as Smoothened and Patched is affected by reduced Arl13b recruitment in these patients (Cevik et al., 2010; He et al., 2018; Larkins et al., 2011; Revenkova et al., 2018). Mutations in *ARL13B* cause classical Joubert syndrome (Cantagrel et al., 2008), and we suggest that the molar tooth formation in Patient 3 with compound heterozygous mutations in *EXOC2* is at least partially due to defects in protein transport within the primary cilia.

Essential roles for EXOC2 have also been revealed in model organisms. In *Drosophila Sec5* (*EXOC2*), null mutants had impaired neuronal membrane traffic that led to failure of neuronal polarization and neuromuscular junction expansion (Murthy et al., 2003). Neurite outgrowth was arrested when the maternal supply of Sec5 was exhausted (Murthy et al., 2003). A *Drosophila Sec15* (*EXOC6*) knockout demonstrates that *Sec15* is critical for a specific vesicle trafficking event that ensures the correct polarized, asymmetrical cell division of progenitor cells and proper cell fate specification (Jafar-Nejad et al., 2005). Furthermore, *Drosophila* Exo70 mutants exhibited impaired integral membrane trafficking to the cell surface, severe neurite outgrowth defects, and reduced synaptic growth at the neuromuscular junction (Koon et al., 2018). All other existing full knockouts of exocyst genes are lethal in mice at the blastocyst stage (reviewed in Martin-Urdiroz et al., 2016). These observations are consistent with our data and with the fact that deletion of the initiation exon of *EXOC2* in the patient fibroblasts dramatically reduces viability of the cells. It is therefore possible that low levels of truncated EXOC2 protein expressed in cells with the p.Arg437* mutation is able to interact through its CorEx domain with other exocyst subunits to facilitate assembly of semi-functional complexes and enable vesicle fusions. We speculate that the truncated EXOC2 binds only weakly but functions catalytically to promote assembly of a hexameric or

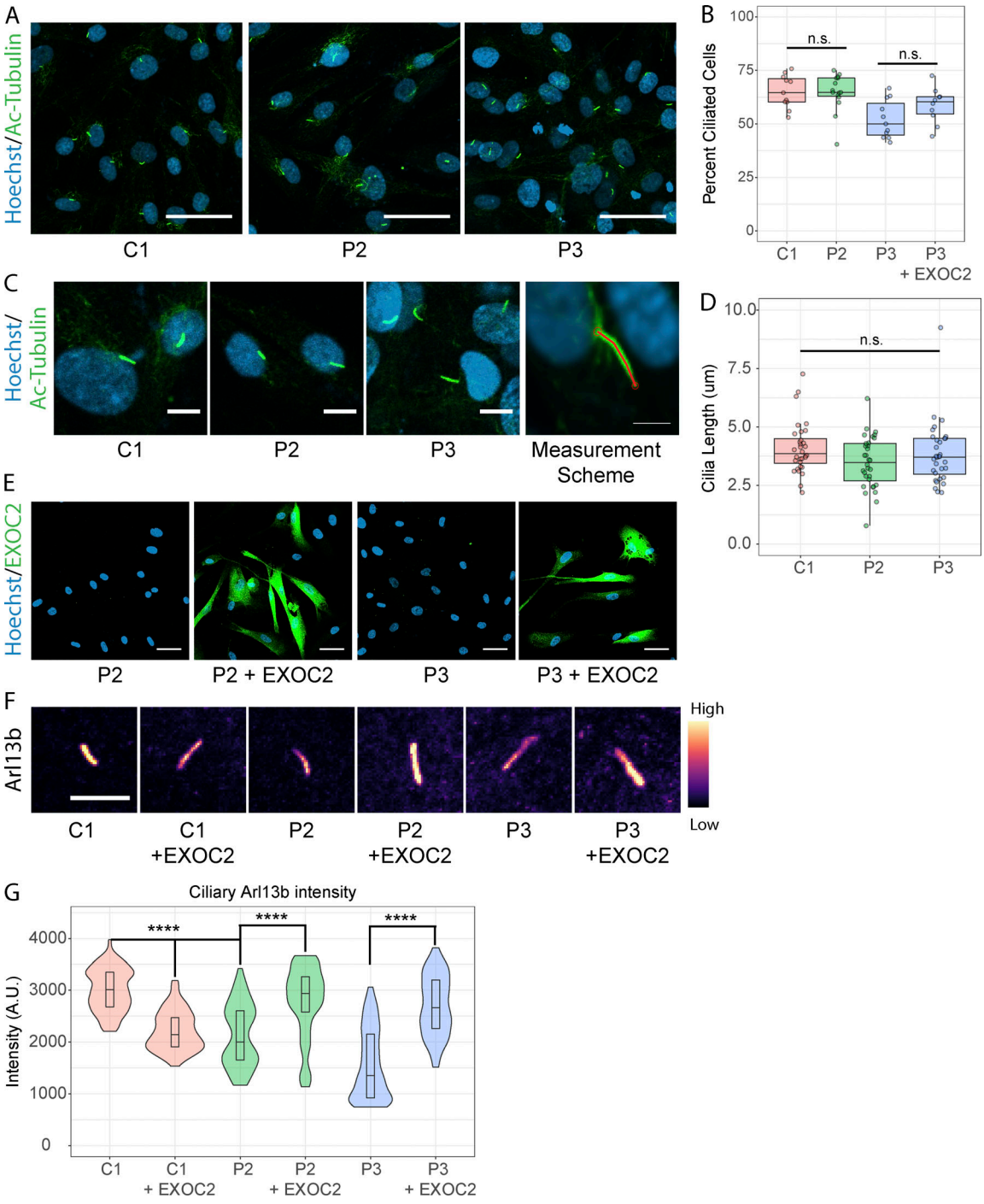


Figure 6. **EXOC2 mutant fibroblasts from patients have defective recruitment of Arl13b to the primary cilia. (A)** Anti–acetyl–α-tubulin staining was used to mark primary cilia in patient fibroblasts. Experiment was repeated three times, and representative images are shown. Hoechst staining was used to demarcate cell nuclei. Scale bar = 50 µm. **(B)** Number of cilia per field was counted. C1 (n = 761), P2 (n = 484), P3 (n = 935), and P3 + EXOC2 wt (n = 514), where n is the total number of cells sampled. **(C)** Close-up of cilia show no significant difference in cilia length between wild-type and EXOC2 mutant cells. Scale bar = 20 µm. Representative of three experiments. **(D)** Measurement of cilia length. Cilia from 32 cells from each condition were measured. **(E)** Wild-type EXOC2 was lentivirally expressed in P2 and P3 variants. Anti-EXOC2 antibodies were used to monitor exogenous EXOC2 protein overexpression. All images were taken at the same acquisition setting as for the P2 sample. This staining was done once to test expression upon generating the stable cell line. Scale bar = 50 µm. **(F)** Arl13b staining and its intensity measurement in the cilia. All images were taken with the same acquisition setting, and intensities were measured from raw unprocessed images. Representative cilia images are shown in pseudo-color to gauge differential intensities in different conditions. LUT legend shows color intensity ranges. All images are of the same scale. Experiment was repeated four times. Scale bar = 20 µm. **(G)** Quantifications of experiment shown in F. Error bars indicate IQR, and line indicates median. P values were calculated using one-way ANOVA and Tukey post hoc analysis. Experiments were performed at least three times. ****, P < 0.0001. n.s., not significant; C1, control; P2, Patient 2; P3, Patient 3; wt, wild-type; LUT, look-up table.

heptameric exocyst complex. The effect of the truncation mutant on the overall structure and stability of the exocyst complex requires further investigation.

In summary, we describe a large consanguineous family with a homozygous variant in *EXOC2*, leading to nonsense-mediated decay of *EXOC2* transcript and a severe reduction in exocytosis and vesicle fusion due to undetectable levels of EXOC2 protein in individuals with the truncating *EXOC2* variant p.Arg437*, which may explain their severe neurological defect. We also describe a second patient with a milder clinical phenotype who harbors compound heterozygous missense variants in *EXOC2* that lead to reduced exocytosis. Together, these findings highlight the importance of the exocyst complex for brain development. Ongoing research is likely to identify other individuals with pathogenic *EXOC2* variants, which will provide invaluable new tools to probe the structure and function of the exocyst complex.

Materials and methods

Patient recruitment

All procedures followed were in accordance with ethical standards and were approved by the human research ethics committee of the respective participating institutes and in accordance with the Helsinki Declaration of 1975, as revised in 2000. Written informed consent was obtained from the parents individually and on behalf of their children. ES was used to identify candidate genes. Two first-degree cousins born from consanguineous marriages (Family 1, Patient 1 [1:IV-2] and Patient 2 [1:IV-8]) were recruited as part of a gene discovery program in children with undiagnosed neurological disease. Potential genes were submitted to Matchmaker Exchange, an international database to match patients of similar phenotype and potential pathogenic variants (Philippakis et al., 2015). An affected patient in Family 2 (Patient 3) was identified through Matchmaker Exchange.

Detailed patient reports

Family 1, Patient 1 (1:IV-2)

Patient 1 was the second-born child to consanguineous Lebanese parents. The pregnancy was complicated by intrauterine growth restriction, leading to elective delivery at 36 wk of gestation. His birth parameters at 36 wk gestation were: weight, 2,025 g (10th centile); length, 47 cm (50th centile); and head circumference (occipital frontal circumference [OFC]), 30 cm (less than third centile).

Dysmorphology: Patient 1 had dysmorphic facial features noted at birth: a small sloping forehead, upslanting palpebral fissures, a high broad nasal bridge, and a broad depressed nasal tip. He had a long flat philtrum and thin upper lip, simple helices, and low-set ears. Patient 1 had deep palmar creases and clenched hands, persistent camptodactyly of fingers, congenital hip dysplasia, broad great toes with hypoplastic second to fifth toenails, and an overriding second toe. He had fine lanugo hair over his back.

Congenital anomalies: Patient 1 had a cardiac abnormality of a ventricular septal defect that was surgically closed. He had bilateral congenital cataracts detected and surgically removed at age 2 yr, with lens replacement. Patient 1 had underdeveloped male external genitalia with a hypoplastic scrotum and undescended testes (left, high scrotal; right, external inguinal ring). He had orchidopexy at age 2 yr.

Poor weight gain and difficulties feeding: Patient 1 had feeding difficulties requiring nasogastric tube feeds from birth, with later fundoplication and insertion of gastrostomy tube and percutaneous endoscopic gastrostomy feeds until age 5 yr. Growth parameters at 5 yr are as follows: height, 101.2 cm (third centile); weight, 15.3 kg (fifth centile). He had poor weight gain and a recurrent aspiration managed by reinsertion of gastrostomy tube at age 8 yr. Height, 121.5 cm (>10th centile for 8-yr-old); weight, 22.3 kg (10th centile for 8-yr-old).

Endocrine: At age 3 mo, Patient 1 presented with increased sodium (serum sodium = 150 mmol/liter) and was diagnosed with partial diabetes insipidus based on a diagnostic water deprivation test. No specific treatment was given. Serum sodium was 145 mmol/liter (n < 145); serum osmolarity was 301 mmol/kg (reference range 265–295 mmol/kg) and random urine osmolality was 179 mmol/kg.

Global developmental delay and postnatal microcephaly: Patient 1 had severe global developmental disability with progressive postnatal microcephaly. He walked at age 4.5 yr and was noted to have increased tone in the lower limbs with limitation of full extension at the knees and hips. He walked with increasingly ataxic gait. He could walk short distances but required a mobility device (stroller) for longer distances and school. He remained nonverbal and not toilet trained. His OFC was 44 cm (less than first centile) at age 5 yr and remained static thereafter (OFC, 44 cm at 8 yr of age).

Seizures: Patient 1 had seizures with onset at age 5 yr, initially with daily focal seizures that progressed to generalized seizures. He was commenced on anticonvulsant medications but experienced increasing seizures with age despite treatment with several anticonvulsants.

Recurrent bacterial infections: At 6 yr of age, Patient 1 had a group A streptococcal septicemia diagnosed on blood culture. The diagnosis was associated with a swollen painful elbow. He frequently had elevated inflammatory marker levels, including elevated erythrocyte sedimentation rate. A diagnosis of Aicardi-Goutières syndrome was considered at 7–8 yr of age. He had recurrent aspiration pneumonia, leading to reinsertion of a gastrostomy tube at age 8 yr.

He died at age 10 yr at home.

Diagnostic investigations: Patient 1 had an electroencephalogram in 2013, which showed right posterior epileptiform foci. MRI of the brain initially at age 1 mo revealed hypoplasia inferior cerebellar vermis and cerebellar hemispheres. There was a normal pituitary bright spot. A scan at 6 yr showed a hypoplastic inferior cerebellar vermis and cerebellar hemispheres; a large fourth ventricle; decreased supratentorial white matter volume and thinning of the corpus callosum; frontal horn cysts; and cerebral atrophy. Patient 1 had a comparative genomic hybridization array at 1 yr of age which identified a heterozygous 8q21.3 deletion (3.2 Mb max). Both parents are heterozygous carriers. The exome sequencing incidental findings included a paternally inherited variant of unknown significance in *IFIH1*

gene (c.1204G>T; p.Glu402*). It should be noted that for *IFIH1*, gain of function variants have been reported in Aicardi-Goutières–like syndromes, not loss of function variants. Patient 1 had diagnostic cerebrospinal fluid neurotransmitter assessments (age 6 yr), and no abnormality was detected (neopterin, 24.3 µmol/mol); previously elevated neopterin measured at age 3 mo was 128.8 µmol/mol). Patient 1 had Angelman syndrome and Prader–Willi syndrome methylation tests, both of which were normal.

Family 1, Patient 2 (1:IV-8)

Patient 2 was born after an uncomplicated pregnancy and delivery. Her birth parameters at 37 wk were: weight, 2,826 g (<50th centile); length, 52.3 cm (>90th centile); and OFC, 32.2 cm (>10th centile).

Progressive microcephaly: Patient 2 had progressive microcephaly. Her OFC at 5 mo was 40 cm (10th centile); length, 63 cm (50th centile); and weight, 6.65 kg (50th centile). Her OFC at 20 mo was 45.3 cm (10th centile); height, 84 cm; and weight, 11.9 kg (50th centile). Her OFC at 4.4 yr was 46 cm (less than first centile).

Physical examination: Physical examination at 20 mo revealed hypertelorism (with an interpupillary distance in the 97th centile); sacral dimple; anteriorly placed anus; normal female external genitalia; slight camptodactyly of fingers; clinodactyly of fifth finger; and bilateral hip dysplasia; and progressive S-shaped scoliosis of upper lumbar spine and lower thoracic spine. Progressive joint contractures have evolved over time and have been managed with orthotics and surgical tenotomy. At the age of 8 yr, she is able to walk with the aid of orthotics.

Gastrointestinal tract: Patient 2 had recurrent diarrhea with patchy inflammation in her stomach and ascending and transverse colon. She has been treated with Salazopyrin since age 7 yr, with a clinical diagnosis of inflammatory bowel disease.

Development: Patient 2 crawled at 20 mo; however, she was unable to pull herself up to stand. She walked at 2.5 yr. She was nonverbal after having a few babble words at 5 mo, which were subsequently lost.

Diagnostic investigations: Patient 2 had an MRI of the brain at 20 mo, which revealed hypoplastic optic discs; generalized decrease myelination; frontal horn cysts; fusion of thalami; and hypoplastic brainstem and cerebellum. She had a single nucleotide polymorphism array (Sureprint G3 Human Comparative Genomic Hybridization [CGH] + SNP array) at 6 yr of age, which revealed an 8q21.3 deletion that was shared with two unaffected siblings, including one who is homozygous for the deletion. Both parents are heterozygous carriers. She had ~7.2% identity by descent over 10 autosomes; and shared only two regions in common with an affected cousin: 8p21.1q12.1 (~34 Mb) and chromosome 20p12.1 (~23.46 Mb). She had shared loss of heterozygosity (LOH) in 8p21.1q12.1; 8q13.3q22.3. The LOH was present in affected cousins, including the deletion region. The other unaffected cousin studied had 9.2% identity by descent over 10 autosomes and eight shared regions of LOH. Exome sequencing revealed a homozygous EXOC2 (chr 6p25.3) that is outside the long segments of LOH. No candidate gene abnormalities were identified within the shared LOH regions. No abnormalities in serum transferrin isoforms were detected. Serum 7-dehydrocholesterol was not detected.

Family 2, Patient 3 (2:II-1)

Patient 3 was a female, born to a nonconsanguineous Italian family. The mother had threatened preterm labor at 34 wk of gestation and had a spontaneous delivery at 37 wk. Her birth parameters were: weight, 2,645 g (25th centile); length, 48 cm (50th centile); OFC, 34 cm (50th centile); Apgar, 10 and 10 at 1 and 5 min, respectively; and she had neonatal jaundice. At 9 mo her growth parameters were: weight, 9,200 g (50–75th centile); length, 69 cm (25–50th centile); and OFC, 47 cm (97th centile).

At age 4 yr, she received a diagnosis of obstructive sleep apnea syndrome with adenotonsillar hypertrophy leading to adenotonsillectomy.

At age 6 yr 3 mo, her growth parameters were: weight, 21.2 kg (50–75th centile); height, 116.5 cm (50th centile); and OFC, 54.6 cm (>98th centile).

Dysmorphology: Patient 3 had an oval face with slight bitemporal hollowing, a high forehead, arched eyebrows, hypertelorism (interpupillary distance at the 97th percentile), low-set simplified ears, thin upper lip with Cupid's bow, lateralized nipples, and slightly dry skin.

Neuropsychological evaluation: Patient 3 had borderline intellectual functioning according to Wechsler Preschool & Primary Scale of Intelligence at 6 yr of age (verbal IQ = 84; performance IQ = 73; full-scale IQ = 75; unchanged at 8 yr). She had good comprehension and adequate lexical understanding. She had poor spontaneous expressive language with incomplete phonetic inventory. She had poor fine and gross motor skills and articulatory difficulties.

Diagnostic investigations: All of Patient 3's routine laboratory testing and metabolic investigations were unremarkable. Electroencephalogram multiple recordings (between age 9 mo and 6 yr) were normal. An MRI of the brain identified a molar tooth cerebellar abnormality, associated with vermis hypoplasia and rhombencephalosynapsis, and abnormal structure of the cerebellar cortical pattern. Patient 3 had an Array-CGH and targeted panel analyses of 28 genes associated with Joubert syndrome and of 82 genes associated with brain malformations; all results were all unrevealing. ES identified compound heterozygosis for two missense *EXOC2* variants: NM_018303.6:c.[389G>A];[1739T>C] (p.[Arg130His];[Leu580Ser]).

Most recent clinical evaluation: Patient 3 attends the second year of primary school with support. An ophthalmological examination was unremarkable. An abdominal ultrasound examination showed a small accessory spleen (8 mm). Overnight pulse oximetry showed oxygen desaturation clusters suggestive of mild obstructive sleep apnea syndrome.

Variant annotation and filtering

Genomic DNA was obtained from whole blood cells from all affected individuals and their available relatives using the QIAamp DNA mini kit (Qiagen), following the manufacturer's instructions.

DNA from Patients 1 and 2, their siblings, and both parents was sequenced using ES and primary bioinformatics processing

that included short sequence read alignment and variant calling on all sequenced samples. Variants were annotated with Annovar (Wang et al., 2010) and filtered based on frequencies from ExAC (Lek et al., 2016), gnomAD (Karczewski et al., 2019 *Preprint*), and the 1000 Genomes Project (Auton et al., 2015). Variants were selected based on the following criteria: amino acid changing (nonsynonymous/stop-gain single-nucleotide variants [SNVs], insertions-deletions, and splicing site variants within 10 bp of exon-intron boundaries); ExAC allele frequency below 1×10^{-5}; predicted to be deleterious in SIFT (Sorting Intolerant From Tolerant), damaging in PolyPhen-2, and conserved in PhyloP; and with balanced alleles for heterozygous calls (depth ratio below 3:1).

For single-sample analysis, homozygous as well as compound heterozygous variants, both indicative of a recessive inheritance, were discarded if the alternative allele's population frequency in the ExAC, 1000 Genomes Project, or internal datasets was >0.5%; heterozygous variants, in this case dominant de novo candidates, were discarded if the alternative allele frequency was >0.1%. Confirmatory Sanger sequencing was completed in genomic DNA samples from all available family members. Multiple alignment of protein sequences was performed using the Uniprot ClustalO alignment tool and Uniprot database sequences.

ES on Patient 3 and both of her parents was done with the SureSelectXT Clinical Research Exome kit (Agilent Technologies) for library preparation and target enrichment. Captured DNA libraries were sequenced by a paired-end 2 × 150–bp protocol on the NextSeq500 (Illumina). Sequencing reads were aligned to the GRCh37/hg19 human genome reference assembly by the BWA software package and then processed by using the Genome Analysis Toolkit suite for base quality score recalibration (Li and Durbin, 2009), realignment of insertion/deletions (InDels), and variant calling, according to Genome Analysis Toolkit Best Practice recommendations (DePristo et al., 2011). Variants annotation was done by VarSeq software (Golden Helix, Inc; v1.4.6), which was also used for family- and frequency-based filtering. Only exonic/splice-site SNVs and coding InDels with MAF <0.01 in the gnomAD v2.1; Karczewski et al., 2019 *Preprint*) were taken into consideration. The potential functional impact of SNVs and InDels was evaluated by the precomputed genomic variants score from dbNSFP (Liu et al., 2011), which was integrated in the annotation pipeline. For selected variants, visual inspection of the quality of reads alignment was done using the Integrative Genomics Viewer (v2.4; Thorvaldsdóttir et al., 2013).

The potential functional impact of SNVs and InDels was evaluated by standard in silico prediction tools SIFT (Kumar et al., 2009), PolyPhen-2 (Adzhubei et al., 2010), and CADD (combined annotation-dependent depletion; Rentzsch et al., 2019). The evolutionary conservation of genomic regions around the variants was analyzed using PhyloP (Cooper et al., 2005).

Confirmatory Sanger sequencing was completed in genomic DNA samples from all available members of both families.

Cell culture

Primary cultures of fibroblasts were established from skin biopsies and cultured in basal medium (high-glucose DMEM [Gibco] with 10% fetal bovine serum [Gibco], 100 units/ml penicillin, and 100 µg/ml streptomycin) at 37°C with 5% CO_2 as previously described (Fowler, 1984; Freshney et al., 2016). PBMCs from Patients 1 and 2 were enriched by Ficoll-Paque separation. Pediatric control fibroblasts were established from healthy children, and control PBMCs were collected from healthy volunteers. All control cell lines and samples were from individuals without any suspected genetic disorders

Cell viability assay

Cells were transfected with guide RNAs as described above. 3 d after transfections, live cells were stained with DAPI, and DAPI-positive cells were counted against the total number of cells seen by brightfield imaging.

Immunoblotting

For denaturing SDS-PAGE gels, fibroblasts were grown to confluency, washed twice in ice-cold PBS, then extracted in radioimmunoprecipitation assay buffer (10 mM Tris-Cl, pH 8.0, 1 mM EDTA, 0.5 mM EGTA, 1% Triton X-100, 0.1% sodium deoxycholate, 0.1% SDS, 140 mM NaCl, 1 mM PMSF, and protease inhibitor cocktail [Roche]) with gentle sonication, and then incubated on ice for 30 min before centrifugation at 20,000 *g* for 20 min at 4°C. Protein concentration was determined from the supernatant using the Pierce BCA Protein Assay Kit. SDS-PAGE was performed on 10–30 µg of cell lysate per sample on Tris-glycine-SDS polyacrylamide gels (Bio-Rad) and then transferred to Amersham polyvinylidene fluoride using standard techniques.

Antibodies were specific to the N-terminus of EXOC2 (1:1,000; ab140620; Abcam) and GAPDH (1:10,000; G9545; Sigma Aldrich). GAPDH was used as a loading control. Primary antibodies were detected with appropriate anti-mouse or anti-rabbit HRP-conjugated antibodies (GE Healthcare) using enhanced chemiluminescence reagents (GE Healthcare) and Amersham Hyperfilm. Protein band intensities were quantified using ImageJ software, and band intensity determined in the linear range was normalized to band intensity of GAPDH.

Immunoprecipitation and Western blot

Cells were grown to confluency in 15-cm dishes, washed twice with ice-cold PBS, and lysed in ice-cold lysis buffer (20 mM Hepes, pH 7.4, 50 mM NaCl, 2 mM EDTA, and 0.2% Igepal CA630) supplemented with protease inhibitor cocktail (cOmplete mini; Roche). Cells were scraped, and lysates were sonicated for 5 s using a probe tip sonicator (Sonics & Materials, Inc.) to ensure complete lysis. Lysates were cleared by centrifugation at 13,000 *g* at 4°C for 10 min. Supernatant was immunoprecipitated using either anti-Exo70 or anti-Sec8 antibodies for 3 h and captured using GammaBind Plus Sepharose antibody purification resin (GE Healthcare). For pull-down experiments, GFP-Trap magnetic beads (ChromoTek) were used. Immunoprecipitated proteins were subsequently analyzed by Western blotting using indicated primary antibodies and secondary antibodies conjugated to IRDye 680RD or 800CW (LI-COR) or HRP. Blots were imaged with Odyssey CLx Infrared Scanner (LI-COR). Anti-Exo70 antibody (immunoprecipitation: 3 µg antibody; Western blot: 1:1,000 dilution) was purchased from Bethyl Laboratories.

Anti-Sec8 antibody (immunoprecipitation: 1 µg antibody; Western blot: 1:1,000 dilution) was from BD Biosciences. Anti-Sec5 rabbit monoclonal antibody (Western blot: 1:1,000 dilution) was from Abcam, and the mouse monoclonal antibody was from Santa Cruz Biotechnology (Western blot: 1:1,000).

Quantitative proteomics

Fibroblasts (300,000 cells) were collected by trypsinization, and cells were washed twice in PBS; then 20 µg of proteins from each sample was lysed, denatured, and digested into peptides with Trypsin and LysC using the PreOmics iST-NIH kit with minor modifications. Alkylated peptides from individual samples were individually labeled with TMT10plex TMTs (Thermo Fisher Scientific) at a ratio of 8 µg tag to 1 µg protein. Samples were then mixed at a 1:1 ratio and peptides purified using the column provided by the PreOmics iST-NIH kit. Following elution and concentration of peptides in a CentriVap Vacuum concentrator (Labconco), 100 µg of pooled peptides was fractioned by offline high-pH fractionation using the Pierce High pH Reversed-Phase Peptide Fractionation Kit (Thermo Fisher Scientific) per manufacturer's instructions, with additional fractions containing 14%, 16%, 19%, and 21% (vol/vol) acetonitrile to a total of 12 fractions. Individual fractions were subsequently concentrated, and peptides were reconstituted in 2% (vol/vol) acetonitrile and 0.1% (vol/vol) TFA. Liquid chromatography–coupled tandem mass spectrometry was performed on an Orbitrap Lumos mass spectrometer (Thermo Fisher Scientific) with a nanoESI interface in conjunction with an Ultimate 3000 RSLC nanoHPLC (Dionex Ultimate 3000). The liquid chromatography system was equipped with an Acclaim Pepmap nano-trap column (Dionex-C18, 100 Å, 75 µm × 2 cm) and an Acclaim Pepmap RSLC analytical column (Dionex-C18, 100 Å, 75 µm × 50 cm). The tryptic peptides were injected to the trap column at an isocratic flow of 5 µl/min of 2% (vol/vol) CH3CN containing 0.1% (vol/vol) formic acid for 5 min, applied before the trap column was switched inline with the analytical column. The eluents were 5% DMSO in 0.1% vol/vol formic acid (solvent A) and 5% DMSO in 100% vol/vol CH3CN and 0.1% vol/vol formic acid (solvent B). The flow gradient was (1) 0–6 min at 3% B; (2) 6–95 min at 3%–22% B; (3) 95–105 min at 22%–40% B; (4) 105–110 min at 40%–80% B; (5) 110–115 min at 80%–80% B; and (6) 115–117 min at 80%–3% and equilibrated at 3% B for 10 min before the next sample injection.

The mass spectrometer was operated in positive-ionization mode with spray voltage set at 1.9 kV and source temperature at 275°C. The mass spectrometer was operated in the data-dependent acquisition mode mass spectrometry spectra scanning from m/z 350 to 1,550 at 120,000 resolution with an AGC target of 4e5. The "top speed" acquisition method mode (3-s cycle time) on the most intense precursor was used, whereby peptide ions with charge states ≥2–5 were isolated with an isolation window of 0.7 m/z and fragmented with high energy collision mode with stepped collision energy of 35% ± 5%. Fragment ion spectra were acquired in Orbitrap at 50,000 resolution. Dynamic exclusion was activated for 30 s.

Raw files were processed using the MaxQuant platform (version 1.6.5.0; Cox and Mann, 2008) and searched against the reviewed UniProt human database (June 2019) containing canonical and isoform sequences using default settings for a TMT 10plex experiment with the following modifications: deamination (of asparagine and glutamine) was added as variable modification, and a mass shift of +113.084 on cysteine was included as a fixed modification per the directions of the PreOmics kit. All modified peptides were used for quantification. Correction factors for the relevant TMT batch were entered into the search parameters. The proteinGroups.txt output from the search was processed in Perseus (version 1.6.5.0; Tyanova et al., 2016). Briefly, $\log_2$-transformed TMT reporter intensity (corrected) values were grouped into control (n = 4 biological replicates) and three technical replicates of Patient 2 (*EXOC2* p.Arg437*) and Patient 3 (*EXOC2* p.Arg130His; p.Leu580Ser). Entries annotated by MaxQuant as "potential contaminant," "reverse," and "only identified by site" were removed from the dataset. Identified proteins were filtered to include 100% valid values across all samples and normalized by subtraction of the median value. Profile plots were generated from the normalized $\log_2$-transformed reporter data. A two-sided t test was performed between control and Patient 2/Patient 3 groups, and significance was determined by P value <0.05 and a fold change of 1.5 ($\log_2$ = 0.585). The results of the t test were expressed as a volcano plot plotted in Prism (version 8.1.2; GraphPad). The mass spectrometry proteomics data have been deposited in the ProteomeXchange Consortium via the PRIDE (Perez-Riverol et al., 2019) partner repository, with the dataset identifier PXD017107.

qPCR analysis

Total RNA was isolated using a commercially available kit (Qiagen RNeasy kit). cDNA was synthesized (GoScript Reverse Transcription Mastermix with random hexamers; Promega). qPCR reactions were performed using custom primers and AccuPower 2X Greenstar qPCR Master Mix (Bioneer Pacific) and a Roche real-time PCR machine.

Plasmid constructs and lentiviral gene rescue

Vamp2-pHluorin used here was described previously (Ahmed et al., 2018). EXOC2 (5′-AGGGGCAGCAGCTTTCAGTC-3′, 5′-CAATCAGGGGAGAAAATCTG-3′) and EXOC4 (5′-CAAAAGCAAAGACCCCTCG-3′) single-guide RNAs were cloned into pLenti-CRISPRv2 plasmid using the BsmBI site.

The human full-length *EXOC2* cDNA clone was obtained from GenScript (pcDNA3.1 containing the NM_018303.6 sequence; GenScript Clone ID OHu25126). *EXOC2* was then amplified from the corresponding *EXOC2*-pcDNA3.1 plasmid using primers containing attB1 and attB2 sites. The PCR products were inserted into the Gateway pDONR221 vector (Thermo Fisher Scientific) through a BP clonase reaction (Thermo Fisher Scientific) to generate the desired entry clones. Lentiviral expression plasmid containing wild-type *EXOC2* was obtained by an LR clonase reaction (Thermo Fisher Scientific) between the *EXOC2* entry vector and the lentiviral destination vector pLX301 (pLX301 was a gift from David Root, Broad Institute of Massachusetts Institute of Technology, Cambridge, MA; Addgene plasmid #25895; Yang et al., 2011) to generate the final *EXOC2*-pLX301 constructs. All vector identities were confirmed by Sanger sequencing. To

generate lentiviral particles, human embryonic kidney 293T cells at ∼70% confluency on 10-cm dishes were cotransfected in fresh basal medium with three plasmids (*EXOC2*-pLX301, the packaging plasmid pCMV-δ8.2, and the pseudotyping plasmid pCMV-VSVG used previously; Calvo et al., 2012) using Effectine reagents (Qiagen). Fresh medium was applied to the cells 16 h after transfection, and after another 24 h of incubation, media supernatants containing packaged virus were harvested and filtered through a 0.45-µm membrane. Primary human fibroblasts at a density of 3×10^5 cells in triplicate 6-well dishes per construct were transduced with viral supernatant along with polybrene (5 mg/ml; Sigma Aldrich) for 48 h. As a negative control, nontransduced cells were treated with puromycin to confirm puromycin sensitivity. As a positive control, nontransduced cells at the same passage number were also expanded in parallel. Transduced cells were grown in antibiotic-free basal medium for 72 h before application of basal medium containing puromycin (1 mg/ml) with daily media change for 7 d, then every 2–3 d for a further 9 d. After at least 16 d of selection, cells were expanded and harvested for various endpoints.

VSVG-GFP ts045 surface exposure assay

Fibroblasts were plated onto sterile coverslips and allowed to attach overnight. The following day, cells were transfected with the VSVG-GFP ts045 construct (a gift from Jennifer Lippincott-Schwartz, Janelia Research Campus, Howard Hughes Medical Institute, Ashburn, VA; Addgene plasmid #11912) using Lipofectamine 3000 (Thermo Fisher Scientific). The following day, cells were transferred to a 5% CO_2 incubator preset at 40°C and left overnight. Cells were then moved to a 5% CO_2 incubator preset at 32°C and left for fixed intervals of 0, 30, 60, or 120 min. Cells were briefly washed with PBS, then immediately fixed in 4% paraformaldehyde for 20 min at room temperature, washed with PBS, and then blocked in 3% BSA in PBS for 1 h at room temperature. Cells were then probed with an antibody against the extracellular domain of VSVG (8G5, Kerafast) at 1:400 for 1 h at room temperature, washed, and then counterstained with goat–anti-mouse IgG-Alexa 594 (Invitrogen) at 1:2,000 for 1 h at room temperature. Coverslips were then mounted with Prolong Gold AntiFade with DAPI (Invitrogen). Images were captured with a Zeiss LSM 780 confocal microscope under a 40×/1.4 oil immersion lens and captured with Zeiss Zen software. Images were analyzed with Fiji Image J software.

In brief, the colocalization was determined by selecting an area of interest encapsulating each cell; then the relative intensity of each pixel from the GFP and Alexa 594 channels within the area of interest was determined. For each image, a second area of interest encapsulating a non–cell-containing area was used to determine the relative background intensity and set the threshold of the background intensity. The background intensity was subtracted from the area of interest for each channel. Then the total intensity across the area of interest for the Alexa 594 channel was divided by the total intensity across the area of interest for the GFP channel.

Transfections

For vesicle fusion experiments, 7×10^5 cells were transfected with 3 µg total cDNA using Human Dermal Fibroblast Nucleofector Kit (Lonza). Amaxa protocol U-022 delivered optimal transfection efficiency and cell survival. Cells were allowed to recover in the cell growth medium as above for 48–72 h after transfection, at which time vesicle fusions could be measured reliably.

Live-cell TIRFM imaging and analysis

The growth media for human fibroblasts were changed to DMEM FluoroBrite supplemented with 10% FBS 30 min before imaging. Cells were imaged using a TIRFM setup under a temperature-controlled environment (Tokai Hit) maintained at 37°C. Images were captured using Photometrics Prime 95B camera mounted on a Nikon Ti-2 microscope using Apo-TIRF 100×/1.49 oil-immersion or Apo-TIRF 60×/1.49 oil-immersion objective. Image acquisition was performed using NIS Elements Advanced Research Imaging software (version 4.60.00 [Build 1171] Patch 02). Images were processed and analyzed with NIS Elements and Matlab. Vesicle fusion events were analyzed by overlaying the time series images to determine all spots and by creating regions of interest around them as described previously (Ahmed et al., 2018). The fluorescence trace over time was extracted and analyzed using Matlab to determine bona-fide fusion events.

Ciliogenesis assays

Cells were plated on Lab-TekII 8-well chamber-slides (Thermo Fisher Scientific). The following day, cell culture medium was changed to DMEM with no serum and grown for an addition 24–48 h to promote ciliogenesis. For rescue experiments, cells were transduced with EXOC2 lentivirus (pLX301-EXOC2) and selected for viral expression with puromycin (3 µg/ml). Cells were fixed in 4% paraformaldehyde and stained using anti–acetyl-α-tubulin (Lys40; 1:1,000; D20G3; Cell Signaling Technology) or anti-Arl13b (1:750; Proteintech) followed by Alexa488-labeled anti-rabbit secondary antibodies. Confocal images were taken using the same acquisition setting from several fields using a Nikon CFI Plan Fluor 40×/1.3 oil immersion objective. For cilia counts, we compared the number of nuclei and cilia in each field for multiple fields. For cilia length, lines were drawn along the shape of the cilia, and the distance from the base to the tip was measured. To assess Arl13b intensity in the cilia, images were thresholded to specifically create binary masks on cilia. To ensure specificity of the masking, objects were confirmed to be associated with a cell nucleus by overlaying with Hoechst stain. Intensities of the individual regions of interest were then recorded using NIS Elements software. To assess successful expression of exogenous wild-type EXOC2 in mutant cells, we stained cells with anti-EXOC2 rabbit monoclonal antibodies (Abcam) followed by Alexa488-labeled rabbit secondary antibodies.

Statistical analysis

Data are reported as interquartile range (IQR) and analyzed by Student's *t* test or one-way ANOVA as indicated using R programming language or Graphpad Prism v7.04.

Data availability

The raw data that support the findings of this study are available from the corresponding author upon request. The mass

spectrometry proteomics data have been deposited in the ProteomeXchange Consortium via the PRIDE (Perez-Riverol et al., 2019) partner repository, with the dataset identifier PXD017107.

Online supplemental material

Table S1 provides elaborate clinical findings of each patient. Table S2 presents the raw proteomics data from EXOC2 patients. Table S3 and Table S4 provide biallelic variants from exome data of Patients 2 and 3, respectively.

Acknowledgments

We thank the Bio21 Mass Spectrometry and Proteomics Facility for the provision of instrumentation, training, and technical support.

The research conducted at the Murdoch Children's Research Institute was supported by the Victorian Government's Operational Infrastructure Support Program. Sequencing, data analysis, and Sanger validation were done at the Garvin Institute, Sydney, Australia. Funding to I.G. Macara was provided by National Institutes of Health grant GM070902, Department of Health and Human Services. We acknowledge funding from the National Health and Medical Research Council (NHMRC Project Grants 1140906 to D.A. Stroud and 116447 to J. Christodoulou and D.A. Stroud; NHMRC Fellowship 1140851 to D.A. Stroud). D.H. Hock is supported by a Melbourne International Research Scholarship. Research at Meyer Children's Hospital, University of Florence was funded by the Seventh Framework Programme, grant agreement no. 602531, DESIRE project. D.H. Hock was supported by the Mito Foundation PhD Top-up scholarship.

Author contributions: N.J. Van Bergen, S.M. Ahmed, M. Cowley, R.C. Dale, D.H. Hock, C. de Caestecker, M. Menezes, S. Massey, G. Ho, T. Pisano, S. Glover, J. Gusman, D.A. Stroud, and M. Dinger: performed experiments and reviewed data. F. Collins, A. Vetro, and R. Guerrini: consulted with patients. N.J. Van Bergen, S.M. Ahmed, I.G. Macara, and J. Christodoulou: wrote the manuscript. All authors reviewed and approved the manuscript.

Disclosures: The authors declare no competing interests exist.

Submitted: 29 October 2019
Revised: 3 February 2020
Accepted: 3 April 2020

References

Adzhubei, I.A., S. Schmidt, L. Peshkin, V.E. Ramensky, A. Gerasimova, P. Bork, A.S. Kondrashov, and S.R. Sunyaev. 2010. A method and server for predicting damaging missense mutations. *Nat. Methods*. 7:248–249. https://doi.org/10.1038/nmeth0410-248

Ahmed, S.M., and I.G. Macara. 2017. The Par3 polarity protein is an exocyst receptor essential for mammary cell survival. *Nat. Commun*. 8:14867. https://doi.org/10.1038/ncomms14867

Ahmed, S.M., H. Nishida-Fukuda, Y. Li, W.H. McDonald, C.C. Gradinaru, and I.G. Macara. 2018. Exocyst dynamics during vesicle tethering and fusion. *Nat. Commun*. 9:5140. https://doi.org/10.1038/s41467-018-07467-5

Armenti, S.T., E. Chan, and J. Nance. 2014. Polarized exocyst-mediated vesicle fusion directs intracellular lumenogenesis within the C. elegans excretory cell. *Dev. Biol*. 394:110–121. https://doi.org/10.1016/j.ydbio.2014.07.019

Auton, A., L.D. Brooks, R.M. Durbin, E.P. Garrison, H.M. Kang, J.O. Korbel, J.L. Marchini, S. McCarthy, G.A. McVean, and G.R. Abecasis; 1000 Genomes Project Consortium. 2015. A global reference for human genetic variation. *Nature*. 526:68–74. https://doi.org/10.1038/nature15393

Bentley, D., and A. Toroian-Raymond. 1986. Disoriented pathfinding by pioneer neurone growth cones deprived of filopodia by cytochalasin treatment. *Nature*. 323:712–715. https://doi.org/10.1038/323712a0

Bergmann, J.E., and S.J. Singer. 1983. Immunoelectron microscopic studies of the intracellular transport of the membrane glycoprotein (G) of vesicular stomatitis virus in infected Chinese hamster ovary cells. *J. Cell Biol*. 97:1777–1787. https://doi.org/10.1083/jcb.97.6.1777

Bröcker, C., S. Engelbrecht-Vandré, and C. Ungermann. 2010. Multisubunit tethering complexes and their role in membrane fusion. *Curr. Biol*. 20:R943–R952. https://doi.org/10.1016/j.cub.2010.09.015

Burack, M.A., M.A. Silverman, and G. Banker. 2000. The role of selective transport in neuronal protein sorting. *Neuron*. 26:465–472. https://doi.org/10.1016/S0896-6273(00)81178-2

Calvo, S.E., A.G. Compton, S.G. Hershman, S.C. Lim, D.S. Lieber, E.J. Tucker, A. Laskowski, C. Garone, S. Liu, D.B. Jaffe, et al. 2012. Molecular diagnosis of infantile mitochondrial disease with targeted next-generation sequencing. *Sci. Transl. Med*. 4. 118ra10. https://doi.org/10.1126/scitranslmed.3003310

Cantagrel, V., J.L. Silhavy, S.L. Bielas, D. Swistun, S.E. Marsh, J.Y. Bertrand, S. Audollent, T. Attié-Bitach, K.R. Holden, W.B. Dobyns, et al; International Joubert Syndrome Related Disorders Study Group. 2008. Mutations in the cilia gene ARL13B lead to the classical form of Joubert syndrome. *Am. J. Hum. Genet*. 83:170–179. https://doi.org/10.1016/j.ajhg.2008.06.023

Cevik, S., Y. Hori, O.I. Kaplan, K. Kida, T. Toivenon, C. Foley-Fisher, D. Cottell, T. Katada, K. Kontani, and O.E. Blacque. 2010. Joubert syndrome Arl13b functions at ciliary membranes and stabilizes protein transport in Caenorhabditis elegans. *J. Cell Biol*. 188:953–969. https://doi.org/10.1083/jcb.200908133

Chien, C.B., D.E. Rosenthal, W.A. Harris, and C.E. Holt. 1993. Navigational errors made by growth cones without filopodia in the embryonic Xenopus brain. *Neuron*. 11:237–251. https://doi.org/10.1016/0896-6273(93)90181-P

Cooper, G.M., E.A. Stone, G. Asimenos, E.D. Green, S. Batzoglou, and A. Sidow; NISC Comparative Sequencing Program. 2005. Distribution and intensity of constraint in mammalian genomic sequence. *Genome Res*. 15:901–913. https://doi.org/10.1101/gr.3577405

Cox, J., and M. Mann. 2008. MaxQuant enables high peptide identification rates, individualized p.p.b.-range mass accuracies and proteome-wide protein quantification. *Nat. Biotechnol*. 26:1367–1372. https://doi.org/10.1038/nbt.1511

DePristo, M.A., E. Banks, R. Poplin, K.V. Garimella, J.R. Maguire, C. Hartl, A.A. Philippakis, G. del Angel, M.A. Rivas, M. Hanna, et al. 2011. A framework for variation discovery and genotyping using next-generation DNA sequencing data. *Nat. Genet*. 43:491–498. https://doi.org/10.1038/ng.806

Dixon-Salazar, T.J., J.L. Silhavy, N. Udpa, J. Schroth, S. Bielas, A.E. Schaffer, J. Olvera, V. Bafna, M.S. Zaki, G.H. Abdel-Salam, et al. 2012. Exome sequencing can improve diagnosis and alter patient management. *Sci. Transl. Med*. 4. 138ra78. https://doi.org/10.1126/scitranslmed.3003544

Doherty, D.. 2009. Joubert syndrome: insights into brain development, cilium biology, and complex disease. *Semin. Pediatr. Neurol*. 16:143–154. https://doi.org/10.1016/j.spen.2009.06.002

Dubuke, M.L., and M. Munson. 2016. The Secret Life of Tethers: The Role of Tethering Factors in SNARE Complex Regulation. *Front. Cell Dev. Biol*. 4:42. https://doi.org/10.3389/fcell.2016.00042

Finger, F.P., and P. Novick. 1997. Sec3p is involved in secretion and morphogenesis in Saccharomyces cerevisiae. *Mol. Biol. Cell*. 8:647–662. https://doi.org/10.1091/mbc.8.4.647

Fogelgren, B., S.Y. Lin, X. Zuo, K.M. Jaffe, K.M. Park, R.J. Reichert, P.D. Bell, R.D. Burdine, and J.H. Lipschutz. 2011. The exocyst protein Sec10 interacts with Polycystin-2 and knockdown causes PKD-phenotypes. *PLoS Genet*. 7. e1001361. https://doi.org/10.1371/journal.pgen.1001361

Fowler, K.J.. 1984. Storage of skin biopsies at -70 degrees C for future fibroblast culture. *J. Clin. Pathol*. 37:1191–1193. https://doi.org/10.1136/jcp.37.10.1191

Freshney, I., A. Capes-Davis, C. Gregory, and S. Przyborski. 2016. Culture of Animal Cells: A Manual of Basic Technique and Specialized Applications. Wiley Blackwell, Hoboken, NJ.

Friedrich, G.A., J.D. Hildebrand, and P. Soriano. 1997. The secretory protein Sec8 is required for paraxial mesoderm formation in the mouse. *Dev. Biol*. 192:364–374. https://doi.org/10.1006/dbio.1997.8727

Fukai, S., H.T. Matern, J.R. Jagath, R.H. Scheller, and A.T. Brunger. 2003. Structural basis of the interaction between RalA and Sec5, a subunit of the sec6/8 complex. *EMBO J.* 22:3267–3278. https://doi.org/10.1093/emboj/cdg329

Gärtner, A., E.F. Fornasiero, and C.G. Dotti. 2015. Cadherins as regulators of neuronal polarity. *Cell Adhes. Migr.* 9:175–182. https://doi.org/10.4161/19336918.2014.983808

Hazuka, C.D., D.L. Foletti, S.C. Hsu, Y. Kee, F.W. Hopf, and R.H. Scheller. 1999. The sec6/8 complex is located at neurite outgrowth and axonal synapse-assembly domains. *J. Neurosci.* 19:1324–1334. https://doi.org/10.1523/JNEUROSCI.19-04-01324.1999

He, K., X. Ma, T. Xu, Y. Li, A. Hodge, Q. Zhang, J. Torline, Y. Huang, J. Zhao, K. Ling, et al. 2018. Axoneme polyglutamylation regulated by Joubert syndrome protein ARL13B controls ciliary targeting of signaling molecules. *Nat. Commun.* 9:3310. https://doi.org/10.1038/s41467-018-05867-1

Heider, M.R., M. Gu, C.M. Duffy, A.M. Mirza, L.L. Marcotte, A.C. Walls, N. Farrall, Z. Hakhverdyan, M.C. Field, M.P. Rout, et al. 2016. Subunit connectivity, assembly determinants and architecture of the yeast exocyst complex. *Nat. Struct. Mol. Biol.* 23:59–66. https://doi.org/10.1038/nsmb.3146

Hirschberg, K., C.M. Miller, J. Ellenberg, J.F. Presley, E.D. Siggia, R.D. Phair, and J. Lippincott-Schwartz. 1998. Kinetic analysis of secretory protein traffic and characterization of golgi to plasma membrane transport intermediates in living cells. *J. Cell Biol.* 143:1485–1503. https://doi.org/10.1083/jcb.143.6.1485

Jafar-Nejad, H., H.K. Andrews, M. Acar, V. Bayat, F. Wirtz-Peitz, S.Q. Mehta, J.A. Knoblich, and H.J. Bellen. 2005. Sec15, a component of the exocyst, promotes notch signaling during the asymmetric division of Drosophila sensory organ precursors. *Dev. Cell.* 9:351–363. https://doi.org/10.1016/j.devcel.2005.06.010

Jin, R., J.R. Junutula, H.T. Matern, K.E. Ervin, R.H. Scheller, and A.T. Brunger. 2005. Exo84 and Sec5 are competitive regulatory Sec6/8 effectors to the RalA GTPase. *EMBO J.* 24:2064–2074. https://doi.org/10.1038/sj.emboj.7600699

Karczewski, K.J., L.C. Francioli, G. Tiao, B.B. Cummings, J. Alföldi, Q. Wang, R.L. Collins, K.M. Laricchia, A. Ganna, D.P. Birnbaum, et al. 2019. Variation across 141,456 human exomes and genomes reveals the spectrum of loss-of-function intolerance across human protein-coding genes. *bioRxiv*. https://doi.org/10.1101/531210 (Preprint posted August 13, 2019).

Kelly, R.B., and E. Grote. 1993. Protein targeting in the neuron. *Annu. Rev. Neurosci.* 16:95–127. https://doi.org/10.1146/annurev.ne.16.030193.000523

Koon, A.C., Z.S. Chen, S. Peng, J.M.S. Fung, X. Zhang, K.M. Lembke, H.K. Chow, C.A. Frank, L. Jiang, K.F. Lau, et al. 2018. *Drosophila* Exo70 Is Essential for Neurite Extension and Survival under Thermal Stress. *J. Neurosci.* 38:8071–8086. https://doi.org/10.1523/JNEUROSCI.0620-18.2018

Kumar, P., S. Henikoff, and P.C. Ng. 2009. Predicting the effects of coding non-synonymous variants on protein function using the SIFT algorithm. *Nat. Protoc.* 4:1073–1081. https://doi.org/10.1038/nprot.2009.86

Larkins, C.E., G.D. Aviles, M.P. East, R.A. Kahn, and T. Caspary. 2011. Arl13b regulates ciliogenesis and the dynamic localization of Shh signaling proteins. *Mol. Biol. Cell.* 22:4694–4703. https://doi.org/10.1091/mbc.e10-12-0994

Lefrancois, L., and D.S. Lyles. 1982. The interaction of antibody with the major surface glycoprotein of vesicular stomatitis virus. II. Monoclonal antibodies of nonneutralizing and cross-reactive epitopes of Indiana and New Jersey serotypes. *Virology*. 121:168–174. https://doi.org/10.1016/0042-6822(82)90126-X

Lek, M., K.J. Karczewski, E.V. Minikel, K.E. Samocha, E. Banks, T. Fennell, A.H. O'Donnell-Luria, J.S. Ware, A.J. Hill, B.B. Cummings, et al; Exome Aggregation Consortium. 2016. Analysis of protein-coding genetic variation in 60,706 humans. *Nature.* 536:285–291. https://doi.org/10.1038/nature19057

Letourneau, P.C.. 1981. Immunocytochemical evidence for colocalization in neurite growth cones of actin and myosin and their relationship to cell-substratum adhesions. *Dev. Biol.* 85:113–122. https://doi.org/10.1016/0012-1606(81)90240-2

Li, H., and R. Durbin. 2009. Fast and accurate short read alignment with Burrows-Wheeler transform. *Bioinformatics.* 25:1754–1760. https://doi.org/10.1093/bioinformatics/btp324

Liljedahl, M., Y. Maeda, A. Colanzi, I. Ayala, J. Van Lint, and V. Malhotra. 2001. Protein kinase D regulates the fission of cell surface destined transport carriers from the trans-Golgi network. *Cell.* 104:409–420. https://doi.org/10.1016/S0092-8674(01)00228-8

Lipschutz, J.H.. 2019. The role of the exocyst in renal ciliogenesis, cystogenesis, tubulogenesis, and development. *Kidney Res. Clin. Pract.* 38:260–266. https://doi.org/10.23876/j.krcp.19.050

Lira, M., D. Arancibia, P.R. Orrego, C. Montenegro-Venegas, Y. Cruz, J. García, S. Leal-Ortiz, J.A. Godoy, E.D. Gundelfinger, N.C. Inestrosa, et al. 2019. The Exocyst Component Exo70 Modulates Dendrite Arbor Formation, Synapse Density, and Spine Maturation in Primary Hippocampal Neurons. *Mol. Neurobiol.* 56:4620–4638. https://doi.org/10.1007/s12035-018-1378-0

Liu, X., X. Jian, and E. Boerwinkle. 2011. dbNSFP: a lightweight database of human nonsynonymous SNPs and their functional predictions. *Hum. Mutat.* 32:894–899. https://doi.org/10.1002/humu.21517

Lobo, G.P., D. Fulmer, L. Guo, X. Zuo, Y. Dang, S.H. Kim, Y. Su, K. George, E. Obert, B. Fogelgren, et al. 2017. The exocyst is required for photoreceptor ciliogenesis and retinal development. *J. Biol. Chem.* 292:14814–14826. https://doi.org/10.1074/jbc.M117.795674

Martin-Urdiroz, M., M.J. Deeks, C.G. Horton, H.R. Dawe, and I. Jourdain. 2016. The Exocyst Complex in Health and Disease. *Front. Cell Dev. Biol.* 4:24. https://doi.org/10.3389/fcell.2016.00024

Mei, K., and W. Guo. 2018. The exocyst complex. *Curr. Biol.* 28:R922–R925. https://doi.org/10.1016/j.cub.2018.06.042

Mei, K., Y. Li, S. Wang, G. Shao, J. Wang, Y. Ding, G. Luo, P. Yue, J.J. Liu, X. Wang, et al. 2018. Cryo-EM structure of the exocyst complex. *Nat. Struct. Mol. Biol.* 25:139–146. https://doi.org/10.1038/s41594-017-0016-2

Mott, H.R., D. Nietlispach, L.J. Hopkins, G. Mirey, J.H. Camonis, and D. Owen. 2003. Structure of the GTPase-binding domain of Sec5 and elucidation of its Ral binding site. *J. Biol. Chem.* 278:17053–17059. https://doi.org/10.1074/jbc.M300155200

Murthy, M., D. Garza, R.H. Scheller, and T.L. Schwarz. 2003. Mutations in the exocyst component Sec5 disrupt neuronal membrane traffic, but neurotransmitter release persists. *Neuron.* 37:433–447. https://doi.org/10.1016/S0896-6273(03)00031-X

Murthy, M., R. Ranjan, N. Denef, M.E. Higashi, T. Schupbach, and T.L. Schwarz. 2005. Sec6 mutations and the Drosophila exocyst complex. *J. Cell Sci.* 118:1139–1150. https://doi.org/10.1242/jcs.01644

Nihalani, D., A.K. Solanki, E. Arif, P. Srivastava, B. Rahman, X. Zuo, Y. Dang, B. Fogelgren, D. Fermin, C.E. Gillies, et al. 2019. Disruption of the exocyst induces podocyte loss and dysfunction. *J. Biol. Chem.* 294:10104–10119. https://doi.org/10.1074/jbc.RA119.008362

Novick, P., C. Field, and R. Schekman. 1980. Identification of 23 complementation groups required for post-translational events in the yeast secretory pathway. *Cell.* 21:205–215. https://doi.org/10.1016/0092-8674(80)90128-2

Pathak, R., V.D. Delorme-Walker, M.C. Howell, A.N. Anselmo, M.A. White, G.M. Bokoch, and C. Dermardirossian. 2012. The microtubule-associated Rho activating factor GEF-H1 interacts with exocyst complex to regulate vesicle traffic. *Dev. Cell.* 23:397–411. https://doi.org/10.1016/j.devcel.2012.06.014

Perez-Riverol, Y., A. Csordas, J. Bai, M. Bernal-Llinares, S. Hewapathirana, D.J. Kundu, A. Inuganti, J. Griss, G. Mayer, M. Eisenacher, et al. 2019. The PRIDE database and related tools and resources in 2019: improving support for quantification data. *Nucleic Acids Res.* 47(D1):D442–D450. https://doi.org/10.1093/nar/gky1106

Philippakis, A.A., D.R. Azzariti, S. Beltran, A.J. Brookes, C.A. Brownstein, M. Brudno, H.G. Brunner, O.J. Buske, K. Carey, C. Doll, et al. 2015. The Matchmaker Exchange: a platform for rare disease gene discovery. *Hum. Mutat.* 36:915–921. https://doi.org/10.1002/humu.22858

Ren, J., and W. Guo. 2012. ERK1/2 regulate exocytosis through direct phosphorylation of the exocyst component Exo70. *Dev. Cell.* 22:967–978. https://doi.org/10.1016/j.devcel.2012.03.005

Rentzsch, P., D. Witten, G.M. Cooper, J. Shendure, and M. Kircher. 2019. CADD: predicting the deleteriousness of variants throughout the human genome. *Nucleic Acids Res.* 47(D1):D886–D894. https://doi.org/10.1093/nar/gky1016

Revenkova, E., Q. Liu, G.L. Gusella, and C. Iomini. 2018. The Joubert syndrome protein ARL13B binds tubulin to maintain uniform distribution of proteins along the ciliary membrane. *J. Cell Sci.* 131. jcs212324. https://doi.org/10.1242/jcs.212324

Rivera-Molina, F., and D. Toomre. 2013. Live-cell imaging of exocyst links its spatiotemporal dynamics to various stages of vesicle fusion. *J. Cell Biol.* 201:673–680. https://doi.org/10.1083/jcb.201212103

Rogers, K.K., P.D. Wilson, R.W. Snyder, X. Zhang, W. Guo, C.R. Burrow, and J.H. Lipschutz. 2004. The exocyst localizes to the primary cilium in MDCK cells. *Biochem. Biophys. Res. Commun.* 319:138–143. https://doi.org/10.1016/j.bbrc.2004.04.165

Roumanie, O., H. Wu, J.N. Molk, G. Rossi, K. Bloom, and P. Brennwald. 2005. Rho GTPase regulation of exocytosis in yeast is independent of GTP

hydrolysis and polarization of the exocyst complex. *J. Cell Biol.* 170: 583–594. https://doi.org/10.1083/jcb.200504108

Seixas, C., S.Y. Choi, N. Polgar, N.L. Umberger, M.P. East, X. Zuo, H. Moreiras, R. Ghossoub, A. Benmerah, R.A. Kahn, et al. 2016. Arl13b and the exocyst interact synergistically in ciliogenesis. *Mol. Biol. Cell.* 27: 308–320. https://doi.org/10.1091/mbc.e15-02-0061

Sommer, B., A. Oprins, C. Rabouille, and S. Munro. 2005. The exocyst component Sec5 is present on endocytic vesicles in the oocyte of Drosophila melanogaster. *J. Cell Biol.* 169:953–963. https://doi.org/10.1083/jcb.200411053

Sztul, E., and V. Lupashin. 2006. Role of tethering factors in secretory membrane traffic. *Am. J. Physiol. Cell Physiol.* 290:C11–C26. https://doi.org/10.1152/ajpcell.00293.2005

Thorvaldsdóttir, H., J.T. Robinson, and J.P. Mesirov. 2013. Integrative Genomics Viewer (IGV): high-performance genomics data visualization and exploration. *Brief. Bioinform.* 14:178–192. https://doi.org/10.1093/bib/bbs017

Tyanova, S., T. Temu, P. Sinitcyn, A. Carlson, M.Y. Hein, T. Geiger, M. Mann, and J. Cox. 2016. The Perseus computational platform for comprehensive analysis of (prote)omics data. *Nat. Methods.* 13:731–740. https://doi.org/10.1038/nmeth.3901

Valente, E.M., B. Dallapiccola, and E. Bertini. 2013. Joubert syndrome and related disorders. *Handb. Clin. Neurol.* 113:1879–1888. https://doi.org/10.1016/B978-0-444-59565-2.00058-7

Vega, I.E., and S.C. Hsu. 2001. The exocyst complex associates with microtubules to mediate vesicle targeting and neurite outgrowth. *J. Neurosci.* 21:3839–3848. https://doi.org/10.1523/JNEUROSCI.21-11-03839.2001

Wan, P., S. Zheng, L. Chen, D. Wang, T. Liao, X. Yan, and X. Wang. 2019. The Exocyst Component Sec3 Controls Egg Chamber Development Through Notch During *Drosophila* Oogenesis. *Front. Physiol.* 10:345. https://doi.org/10.3389/fphys.2019.00345

Wang, K., M. Li, and H. Hakonarson. 2010. ANNOVAR: functional annotation of genetic variants from high-throughput sequencing data. *Nucleic Acids Res.* 38. e164. https://doi.org/10.1093/nar/gkq603

Wu, H., C. Turner, J. Gardner, B. Temple, and P. Brennwald. 2010. The Exo70 subunit of the exocyst is an effector for both Cdc42 and Rho3 function in polarized exocytosis. *Mol. Biol. Cell.* 21:430–442. https://doi.org/10.1091/mbc.e09-06-0501

Xu, Y., B.R. Rubin, C.M. Orme, A. Karpikov, C. Yu, J.S. Bogan, and D.K. Toomre. 2011. Dual-mode of insulin action controls GLUT4 vesicle exocytosis. *J. Cell Biol.* 193:643–653. https://doi.org/10.1083/jcb.201008135

Yang, X., J.S. Boehm, X. Yang, K. Salehi-Ashtiani, T. Hao, Y. Shen, R. Lubonja, S.R. Thomas, O. Alkan, T. Bhimdi, et al. 2011. A public genome-scale lentiviral expression library of human ORFs. *Nat. Methods.* 8:659–661. https://doi.org/10.1038/nmeth.1638

Yeaman, C., K.K. Grindstaff, J.R. Wright, and W.J. Nelson. 2001. Sec6/8 complexes on trans-Golgi network and plasma membrane regulate late stages of exocytosis in mammalian cells. *J. Cell Biol.* 155:593–604. https://doi.org/10.1083/jcb.200107088

Zuo, X., W. Guo, and J.H. Lipschutz. 2009. The exocyst protein Sec10 is necessary for primary ciliogenesis and cystogenesis in vitro. *Mol. Biol. Cell.* 20:2522–2529. https://doi.org/10.1091/mbc.e08-07-0772

Zuo, X., G. Lobo, D. Fulmer, L. Guo, Y. Dang, Y. Su, D.V. Ilatovskaya, D. Nihalani, B. Rohrer, S.C. Body, et al. 2019. The exocyst acting through the primary cilium is necessary for renal ciliogenesis, cystogenesis, and tubulogenesis. *J. Biol. Chem.* 294:6710–6718. https://doi.org/10.1074/jbc.RA118.006527

Supplemental material

Tables S1–S4 are provided online as separate Excel files. Table S1 provides comprehensive clinical findings of affected family members with *EXOC2*-related neurological disorder. Table S2 provides proteomics data on EXOC2 patients, including data used to generate Volcano plots and profile plots of log_2-transformed normalized TMT reporter intensities for cellular proteins in Patients 2 and 3 replicates and control fibroblasts. Table S3 shows biallelic variants from exome data of Patient 2 filtered following a recessive inheritance pattern. Table S4 shows biallelic variants from exome data of Patient 3 filtered following a recessive inheritance pattern.